Detection and reconstruction of rock glaciers kinematics over 24 years (2000-2024) from Landsat imagery

Diego Cusicanqui[1], Pascal Lacroix[1], Xavier Bodin[2], Benjamin Aubrey Robson[3], Andreas Kääb[4] and Shelley MacDonell[5,6]

[1]Institut des Sciences de la Terre (ISTerre) CNES, CNRS, IRD, Univ. Grenoble Alpes, Grenoble, 38000, France
[2]Laboratoire EDYTEM, Univ. Savoie Mont-Blanc, Le Bourget du Lac, 73376, France
[3]Department of Earth Science, University of Bergen, Bergen, Norway
[4]Department of Geosciences, University of Oslo, Oslo, 0316, Norway
[5]Centro de Estudios Avanzados en Zonas Áridas (CEAZA), La Serena, Chile
[6]Waterways Centre, University of Canterbury and Lincoln University, Christchurch, New Zealand

Correspondence to: Diego Cusicanqui (diego.cusicanqui@univ-grenoble-alpes.fr)

Abstract. Rock glacier velocity is now widely acknowledged as an Essential Climatic Variable for permafrost. However, representing decadal regional spatio-temporal velocity patterns remains challenging due to the limited number of high-resolution (<5 m) remote sensing data. Medium resolution satellite data (10-15 m) is on the contrary globally available over several decades, and has never been used for rock glacier kinematics. This study presents a robust methodological approach based on the pairwise feature tracking image correlation using medium-resolution Landsat 7/8 optical imagery together with the inversion of surface displacement time series and the automatic detection of persistent moving areas (PMA) applied to rock glacier monitoring in the Semi-Arid Andes of South America. This methodology enables the detection and quantification of surface kinematics of 382 gravitational slope mass movements (153 corresponding to rock glaciers) over a 24-years, over an area of 2250 km². This is the first time that Landsat images have been used to quantify rock glacier displacements and derive velocities. From this we derive an average velocity of 0.37 ± 0.07 m a^{-1} over 24 years for all rock glaciers, with some exceptions where large rock glaciers and debris frozen landforms exhibit surface velocities exceeding 2 m a^{-1}. The results of this study show a good agreement with high-resolution imagery and recent in-situ measurements, however the L7/8 imagery-derived velocities are on average underestimated by approximately 20-30%. Additionally, the relatively high uncertainties between consecutive image pairs make it challenging to interpret annual velocity variations. Nevertheless, decadal velocity changes were observed in 3% of PMAs, where three rock glaciers showing 11% increase and six rock glaciers showing an 18% decrease in velocity over one decade. Our study suggests a control of velocity mostly based on the rock glacier size, as well as the orientation, slope and elevation controls the position of the active zones, suggesting that permafrost thaw influences the location of high-altitude landslides in the Andes. This study demonstrates the feasibility of using medium-resolution optical imagery for monitoring rock glaciers globally over several decades.

1 Introduction

Historically, the state of the cryosphere has been measured using specific variables defined by Global Climate Observing System (GCOS) (GCOS, 1995) such as mass balance for glaciers, snow cover variability for snow and ground temperature for permafrost. Among those variables, glacier mass balance and snow cover variations are relatively well known at a global scale (Hugonnet et al., 2021; Notarnicola, 2020) compared to changes in mountain permafrost, which are still very incompletely monitored (Bolch et al., 2020).

Permafrost is an important component of the cryosphere occurring at high latitudes (i.e. polar regions) and high elevations (i.e. mountainous areas). As permafrost —ground material remaining at or below 0°C for at least two consecutive years— is a thermal phenomenon, it is thus sensitive to changes in climate forcing (Hock et al., 2019). The evidence of mountain permafrost warming relies on very few direct borehole observations (Noetzli et al., 2019), distributed mostly in the western Alps and Alaska. Thus, several mountain ranges are lacking sufficient permafrost monitoring data to analyse changes. Mountain permafrost degradation is indicated by the increase in ground temperatures and active layer thickness (Etzelmüller et al., 2020), the increase of liquid water content within the frozen terrain (Cicoira et al., 2019), as well as ground-ice melt (Cusicanqui et al., 2021; Haberkorn et al., 2021). However, warming affects mountain permafrost differently according to the type of terrain, reflecting in particular the influence of snow cover on the ground. While a rather steady warming trend can be observed in steep rock slopes (Magnin et al., 2024), where snow is poorly present, permafrost temperatures in loose rock formations such as rock glaciers show pronounced inter-annual variations, mostly due to the variable insulating effect of snow (Thibert & Bodin, 2022; Kellerer-Pirklbauer et al., 2024).

In the present paper, we follow the definitions proposed by the IPA Rock Glaciers Inventory and Kinematics (RGIK) action group, stating that rock glaciers can be defined as “debris landforms generated by the former or current creep of frozen ground (permafrost), detectable in the landscape with the following morphologies: front, lateral margins and optionally ridge-and-furrow surface topography” (Berthling, 2011; RGIK, 2023). Given the complexity of measuring permafrost warming, rock glacier velocity has been recently proposed and accepted by the GCOS to be a complement of the Essential Climatic Variable ECV-permafrost (Hu et al., 2023). Indeed, the thermally-dependent creep of ice-rich frozen ground is inherently sensitive to climatic conditions and it is able to change over different timescales (Delaloye et al., 2010; Kääb et al., 2007; Sorg et al., 2015). While the variation of creep velocities at inter-annual, seasonal and over shorter time-scales reflects mainly the influence of weather (Kenner et al., 2017; Wirz et al., 2016), long-term patterns — decadal to pluri-decadal scales— relate primarily to mean annual air or ground temperatures (Pellet et al., 2022, Kellerer-Pirklbauer et al., 2024).

Since the early 2000s, there has been a growing interest from the international community in the monitoring of rock glacier velocity. Indeed, observations show that rock glacier velocities often exhibit similar interannual to longer term trends at a regional scale (Kellerer-Pirklbauer & Kaufmann, 2021; Marcer et al., 2021; Pellet et al., 2022), which strongly depends on local ground temperature changes (Noetzli et al., 2019). The velocity of rock glaciers is controlled by the intrinsic characteristics of the landform, in particular its internal structure (ice / debris proportions, thickness) and the topography (slope of the bed), but it is also influenced substantially by a external climatically-driven factors such as ground temperature and advection, infiltration, or internal meltwater production and routing (Jansen and Hergarten, 2006; Cicoira et al., 2019a; Kenner et al., 2020). Thus, the magnitude and variability of velocity can give an indication as to the current state and possible ongoing changes in the characteristics of the permafrost body. The monitoring of changes in rock glacier velocity thus provides information about the impact of climate change on mountain permafrost kinematics and, indirectly, on its thermal state. Given the observed current warming context of mountain permafrost (Noetzli et al., 2019), creep speed of rock glaciers in cold mountains is expected to increase with ground temperature (Arenson et al., 2015; Kääb et al., 2007; Müller et al., 2016).

Quantifying rock glacier velocity over regional scales has been most successfully achieved using satellite radar interferometry (InSAR) data. This method enables the detection of slow slope movement (i.e. rock glacier motion) in the Line of Sight (LOS) of the satellite, over large regions and hundreds of individual landforms (Hu et al., 2023). This approach has been used to map rock glacier motion around the world (Bertone et al., 2022). This data source has served as a base for classifying movements rates of various orders of magnitude (cm/d, cm/month, dm/month, cm/a, etc.), recently standardised within the RGIK group (RGIK, 2023). However, even if this technique is well suited for rock glacier mapping (Barboux et al., 2014) satellite radar interferometry is most suitable for relatively slow rock glacier speeds, with maximum speeds of approximately 1–1.5 m a^{-1} observed over short observation periods (6, 12 days). Beyond this threshold, InSAR signals become geometrically decorrelated and thus uninterpretable (Villarroel et al., 2018). In addition, freely available SAR data with high temporal resolution has only been available since the early 21st-century (Strozzi et al., 2020). This means that no climatic timescales (i.e. decennial timescales) for rock glaciers can be obtained with this source of data.

Comparatively, optical imagery offers a more robust alternative where feature tracking techniques can be applied to repeat imagery to derive surface displacements, both to contemporary imagery and historical datasets, allowing rock glacier velocities to be investigated over longer time-scales (Cusicanqui et al., 2021; Kääb et al., 2021; Kaufmann et al., 2021). This technique is not well suitable for slow velocities due to its low signal-to-noise ratio (unless very high spatial resolution allows tracking the movement), but rather well suited for medium to large movements beyond 1 - 1.5 m a^{-1} (Hartl, et al., 2021; Marcer et al., 2021). However, to date, such techniques have been exemplified on rock glaciers using high resolution optical imagery (<5 m). Very often, using airborne imagery that is not easily accessible, can be prohibitively expensive for larger regions or for more extensive time series. As a consequence, few periglacial areas have been extensively investigated

using feature tracking, with most of the studies restricted to the European Alps (Cusicanqui et al., 2021; Hartl et al., 2016; Kellerer-Pirklbauer and Kaufmann, 2012), some isolated regions in the Andes i.e. Tapado rock glacier (Vivero et al., 2021; Blöthe et al., 2021), in northern Tien Shan (Kääb et al., 2021) and more recently in the United States (Kääb and Røste, 2024).

Medium resolution imagery (Landsat-4/5/7/8, SPOT 1-4, ASTER) has offered a continuous dataset for monitoring slow-moving landforms since the 1980's. Recent progress in time-series processing has enabled the development of methods for both detecting and monitoring slow-moving landslides using medium-resolution imagery over the last 40-50 years (Bontemps et al., 2018; Lacroix et al., 2020a). These methods have never been used for rock glaciers because of (1) the rather slow motion of rock glaciers overall (~ 1 m a^{-1}), and (2) the difficulty of the processing caused by the presence of snow and shadows in mountain topography. Here, we demonstrate the applicability of the free and open-access, global, medium-resolution satellite datasets Landsat 7/8 (called hereafter L7/8) to characterise rock glacier displacements and velocity for the early 21th century in a region of the semiarid Andes (both on Chile and Argentina). We further validate our results at a regional scale using Sentinel-1 wrapped interferograms, and at a more local scale with very high resolution (called hereafter VHR) datasets e.g. Geoeye, Pléiades, airborne on the Tapado complex area and recent Global navigation satellite system (GNSS) measurements.

2 Study area and previous work

Our study area is located within the Coquimbo and San Juan provinces, in the semiarid Andes of Chile and Argentina (between 29°20'S and 31°15'S latitude; Fig. 1). It is a ~45x45 km² site, with altitudes ranging between 3,000 and 6,300 m above sea level (a.s.l). The regional climate is characterised by semiarid conditions, influenced mainly by the subtropical South Pacific anticyclone (Montecinos & Aceituno, 2003). The rugged topography from coastal position to the high elevation of Andes mountain range (~6,000 m.a.s.l.) have a strong influence on the general atmospheric circulation, notably differentiating the eastern and western climatic systems (Kalthoff et al., 2002). Schauwecker (2022) shows that the precipitation coming from the humid Pacific masses occurs almost exclusively as snowfall and mostly concentrated in the austral winter, between May and August. Year-to-year precipitation varies notably in accordance with the El Niño Southern Oscillation (ENSO) phenomenon with above (below) -average precipitation during El Niño (La Niña) events (Masiokas et al., 2006, 2010) with recent deficits in precipitations between 20-40% (Garreaud et al., 2020). Recent meteorological records on three Automatic Weather Stations (AWS) show mean annual precipitation of ~170 mm in the last decade (CEAZA, 2023). Recent studies of the air temperature have shown a warming trend of 0.2°C per decade in the central Andes, closely influencing the decrease in snowfalls (Poblete & Minetti, 2017; Réveillet et al., 2020).

According to global permafrost distribution models (Gruber, 2012; Obu, 2021) and a local one (Azócar et al., 2017), heterogeneous/discontinuous permafrost is present between 3,900 - 4,500 m a.s.l., becoming more prevalent above 4,500 m a.s.l. (Fig. 1). In this context, several rock glacier inventories have been carried out along the Chilean (DGA, 2022) and Argentinian (IANIGLA, 2018) Andes as well as several detailed/local geomorphological investigations (Monnier & Kinnard, 2015, 2016, Halla et al., 2021; Navarro et al., 2023; de Pasquale et al., 2022). According to both inventories of Chile and Argentina, both of which are based on geomorphological interpretation of optical satellite imagery, the area has a relatively high number of rock glaciers with 80 located on the Chilean side and 235 on the Argentinian side (Fig. 1). The study of mountain permafrost in this particular region of the semiarid Andes has received attention during the last decades because of the high density and large extension of rock glaciers (Janke et al., 2015). Most recent studies highlight the complex interaction between remnants of glaciers, debris covered glaciers and rock glaciers (Navarro et al., 2023a; Robson et al., 2021) as well as the importance of rock glaciers as water storage resources (MacDonell et al., 2022; Schaffer et al., 2019; Schaffer and MacDonell, 2022).

Despite this interest, a limited overview of the status of rock glacier velocities exist, while historical trends of velocity largely remain unknown. For instance, Villarroel et al. (2018) provided a recent kinematic inventory of the Argentinean Andes, between 30.5°S and 33.5°S, identifying ~2100 active rock glaciers based on InSAR. On the other hand, Blöthe et al (2021) provided a regional assessment in the “Cordon del Plata” range (~300 km south of our study area), quantifying velocity fields of 244 rock glaciers between 2010 and 2017/18 using offset tracking optical imagery. Only two rock glaciers monitoring in this region are monitored i.e. Dos Lenguas rock glacier studied mostly with InSAR (Strozzi et al., 2020) and more recently with Uncrewed Aerial Vehicle (UAV; Stammler et al., 2024) in Argentina and Tapado complex in Chile (Vivero et al., 2021), monitored with GNSS data since 2009 and with historical aerial images, being the only providing the longest surface velocity time series since the 1950's. In this sense, a historical perspective is still lacking in the region. Finally, this region was chosen due to good coverage of reference datasets, namely VHR satellite imagery and in situ GNSS measurements on the Tapado rock glacier (DGA, 2010), that could be used for validation.

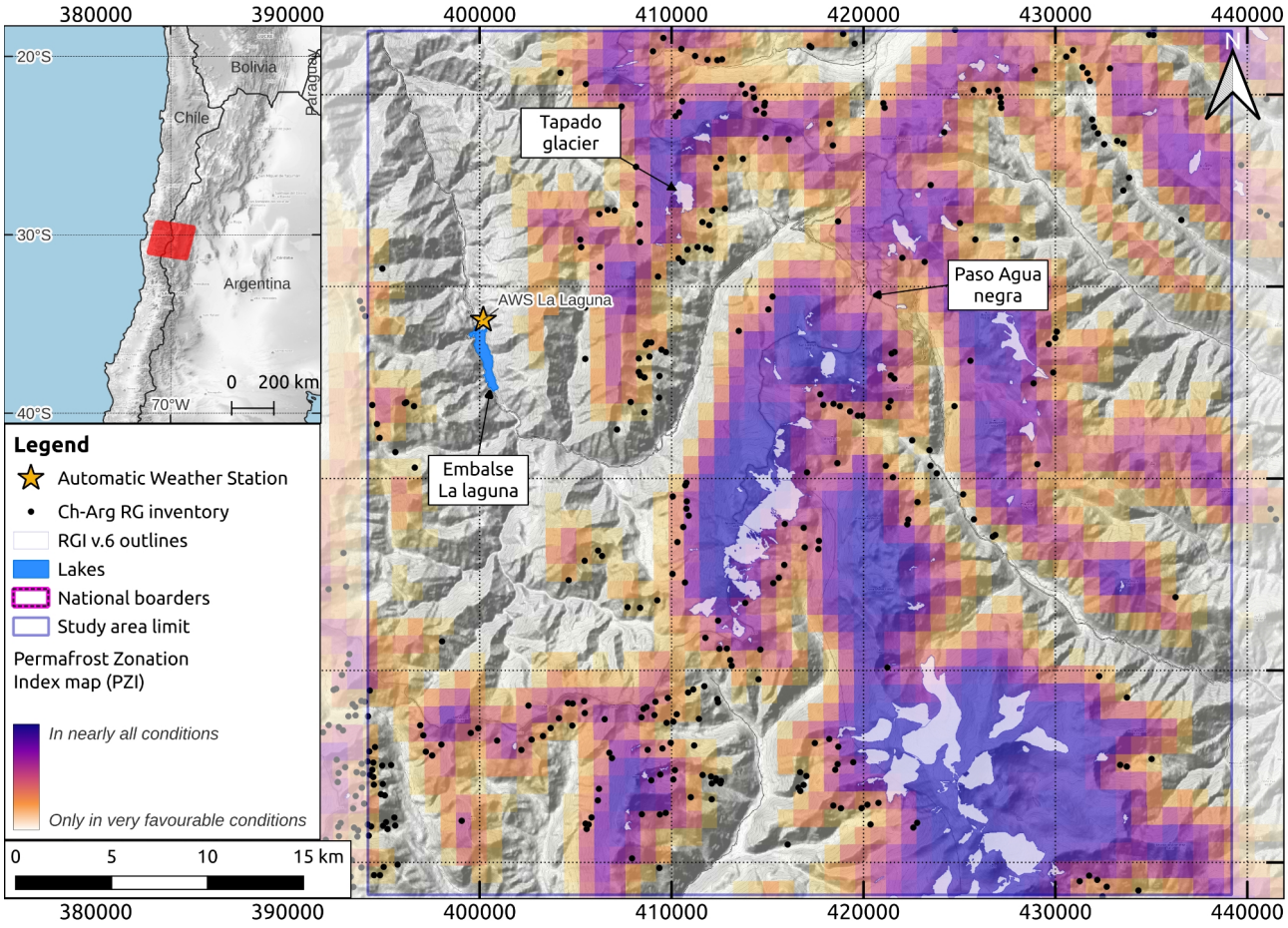

Figure 1: Location of the study area in the semiarid Andes (between 29°20'S and 31°15'S latitude). Red square in the inner map shows the footprint of the Landsat scenes used in this study. Within the main map, black dots correspond to rock glacier inventory for Chile (DGA, 2022) and Argentina (IANIGLA, 2018). The orange-purple colorbar represents the Permafrost Favorability Index (PFI) from (Gruber, 2012). A comparison with the more recent PFI from Obu (2021) is shown in Fig. S1. Background map corresponds to © OpenTopoMap.

3 Data

Three different remote sensing datasets were used in this study: (1) L7/8 images, (2) VHR images from airborne platforms and satellites, used to validate the L7/8 products temporally, and (3) Sentinel-1 SAR interferograms, used to validate the L7/8 products spatially. We also used GNSS data acquired on one specific rock glacier for the kinematic validation.

3.1 L7/8 dataset

The L7/8 dataset comprises freely and open available 8-band multispectral orthorectified satellite images spanning the period from 2000 to 2024 (Fig. 2a and b). We used only the L7/8 panchromatic band (B8) with the highest spatial resolution (15 m). However, due to the Scan Line Corrector failure on the Landsat-7 satellite between 2004 and 2013 (Markham et al., 2004), we excluded Landsat-7 scenes within this period to avoid data gaps. All images correspond to path and row 233 / 081 and have been cropped within a common grid (3001x3001 pixels) corresponding to a surface area of 45x45 km². One image per year was chosen visually during the summer (January to April), with the goal of obtaining the least snow and cloud cover possible (Table S1).

3.2 VHR dataset

The VHR dataset comprises high-resolution satellite orthoimages acquired at irregular intervals between 2000 and 2020 (Fig. 2b). These images comprise a combination of data from three different sensors, namely aerial (0.5 m), Geoeye (0.5 m) and Pleiades (0.5 m). In this dataset, the panchromatic images have been orthorectified and resampled within the same grid with a spatial resolution of 1x1 m. Given the variable spatial coverage of the VHR datasets, we have selected two sub-areas (i.e. Tapado and Largo RG sub-regions, respectively; Fig. 2) where the largest amount of imagery is available attempting to maintain temporal coverage comparable to that of the L7/8 dataset.

With regard to the processing of the VHR dataset, the majority of the images were already orthorectified and used directly from Robson et al., (2022), except for: (i) the photogrammetric flight in 2000's and ii) the 2014 Pleiades acquisition. Regarding the 2000's photogrammetric flight, we undertook a re-processing of the data by extending the area to the Largo rock glacier (4 km north from Tapado complex area; Fig. 2d) which was not initially covered in Robson et al., (2022). The photogrammetric processing was based on the method set out by Cusicanqui et al., (2021) using Agisoft Metashape software v. 2.0.3 (Smith, 2011). Sixteen Ground Control Points (GCPs) were used around both small sub-areas. The 2019 Pleiades DEM has been employed as a reference for the GCPs (Robson et al., 2022). A coregistration stage using Nuth & Kääb (2011) methodology was undertaken to correct small shifts of the 2000's aerial DEM.

With regard to the Pléiades 2014 acquisition, we applied the same methodology described in Cusicanqui et al., (2023) to process the Pléiades 2014 stereo pair without GCP's and using only Rational Polynomial Coefficients (RPC). The 2014 stereo DEM was coregistered afterwards on the 2019 Pléiades DEM. Subsequently, the orthoimages were adjusted in accordance with the aforementioned DEM co-registration values. Finally, VHR images were acquired during the dry season between November to April, spanning almost two decades (Table S1).

Figure 2: a) and b) Spatial extent and temporal distribution of L7/8 and VHR datasets, respectively; c) and d) Zoom over high resolution sub-regions used for validation. Orange polygons represent the 2013 rock glacier inventory from DGA,

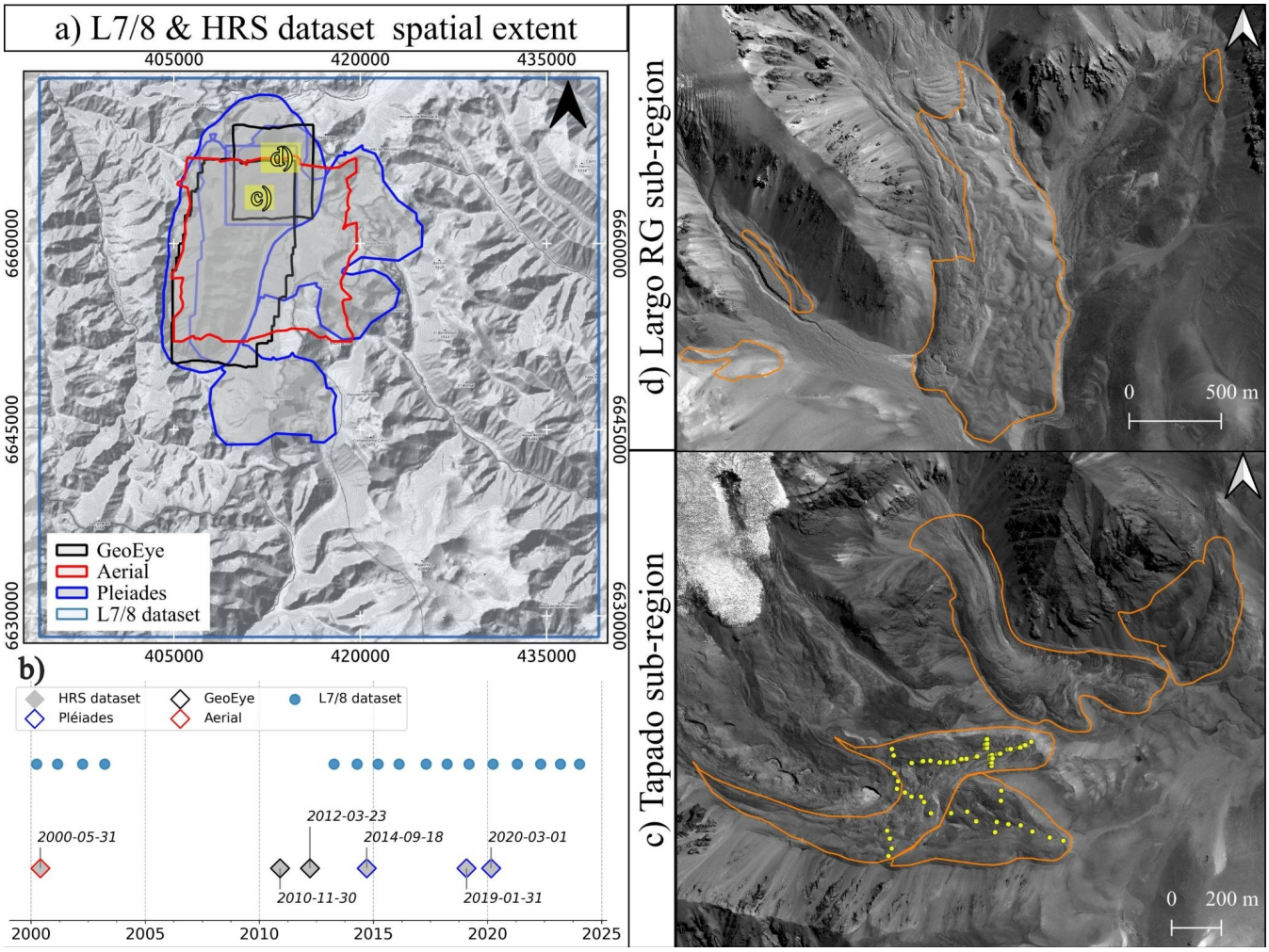

(2010) and yellow-dots represent the GNSS network on the Tapado complex (CEAZA, 2023). Image backgrounds correspond to © OpenTopoMap for a) and Pléiades 2019 imagery © CNES/AIRBUS for c) and d).

3.3 Sentinel-1 interferograms

Due to the limited spatial extent of the VHR dataset, we used raw Sentinel-1 wrapped interferograms for validate L7/8 surface displacement products (cf. Section 4.1) as well as for classifying the inventory of gravitational mass movements including rock glaciers and landslides (cf. Section 4.3). This analysis was conducted through a visual inspection of several interferograms covering the entire study area. Sentinel-1 interferograms were processed using the ForM@Ter LArge-scale multi-Temporal Sentinel-1 InterferoMetry processing chain —FLATSIM— service (Thollard et al., 2021) at different temporal baselines i.e. 12, 60 and 360 days. For this study, we employed 40 interferograms from early winter 2022 until late winter 2023 in both ascending and descending orbits (path 120 and 156, respectively; Table S2). Those interferograms were averaged in 2-looks (2 pixels in azimuth, 8 pixels in range) in radar geometry, equivalent to 30 metres in terrain geometry. In

brief, the FLATSIM service systematically produces interferograms from Sentinel-1 data and displacement time series, over large geographical areas. This service is based on the InSAR "New Small temporal and spatial BASelines" (NSBAS) processing chain as described in Doin et al., (2011) and Grandin (2015). FLATSIM products were corrected topographically using a SRTM-DEM and atmospherically corrected using ERA-5 atmospheric model mapped on the DEM. Full details can be found in Thollard et al., (2021) and ForM@TER platform.

3.4 GNSS data

The surface kinematics of the Tapado rock glacier have been measured by the Centro de Estudios Avanzados en Zonas Áridas (CEAZA). This network consists of a survey of 61 points measured since 2009 using a differential GNSS (dGNSS) system (DGA, 2010). According to CEAZA (2012, 2016) and Vivero et al. (2021), the base station coordinates were fixed using the Trimble CenterPoint RTX post processing service, and the differential post processing of the GNSS raw data between this base and the rover GNSS antenna was conducted using Trimble Business Center (TBC, V.4) surveying software. The reported average horizontal and vertical precisions (95%) were 0.02 and 0.04 m, respectively. In order to address some inconsistencies on point locations i.e. points systematically shifted few metres in north-east direction, 14 groups of GNSS points corresponding to the same block and specific dates (i.e. 2013-12-11, 2022-04-06, 2010-12-06) were removed from the original dataset. The remaining dataset comprises 47 groups of points and has been employed primarily for the validation of surface velocity maps derived from both L7/8 and VHR dataset (cf. Section 5.3). Additionally, as no GCPs exist for Largo rock glacier, we manually tracked 13 pseudo-GCPs on representative features clearly identified on the VHR dataset to compare with L7/8 dataset (cf. Section 5.3).

4 Methods

The methodology employed in this study is based on the feature tracking offset image correlation strategy, which involves the analysis of a large number of images available for a site. Subsequently, inversion of time-series techniques were applied to the correlated images in order to derive consistent surface displacement fields over time (Section 4.1). Then, a medium-resolution DEM was used to identify Persistent Moving Areas (PMAs) along the slope direction within the study region (Section 4.2). Eventually, we validate the final surface velocity fields by comparing them to recent dGNSS measurements and feature tracking of both L7/8 & VHR datasets on two small sub-regions in the upper regions of the La Laguna catchment (i.e. Tapado region).

4.1 Inversion of displacement time-series

Horizontal displacement time series were derived from L7/8 and VHR orthorectified images, following a similar approach developed in Bontemps et al., (2018), previously applied on slow moving landslides (Lacroix et al., 2019). The method used in in this study is summarized as follows:

a) Feature tracking image correlation was performed in all possible pairwise combinations and their permutations (i.e. forward and backward). Two different software were used for each dataset. Firstly, we used Mic-Mac (Rupnik et al., 2017) through the Normalised Cross Correlation (NCC) algorithm to correlate images within the L7/8 dataset. This software was selected for its ability to handle images with low radiometric contrast and for small objects (Lacroix et al., 2020b). Secondly, the Ames Stereo Pipeline (ASP) (Beyer et al., 2018) was employed to correlate image pairs within the VHR dataset. In ASP, the More Global Matching (MGM) implementation (Facciolo et al., 2015) was used to perform image correlation. MGM algorithm reduces high-frequency spatial artefacts (compared to classic NCC algorithms) in textureless regions and produces smooth surface displacement fields. Image mismatches associated with georeferencing errors are minimised due to the pre-alignment strategy (i.e. automatic identification of image features matched in a pair of images used then as tie-points) before the feature tracking stage. Both softwares present an adaptive windows matching strategy corresponding to 3x3 for MicMac and 7x7 for ASP as the smallest window size.

b) In both cases, all pixels with low correlation coefficient values (CC < 0.6) and displacement magnitude > 120 m, were masked. Furthermore, an additional glacier outline masking step was applied to the VHR dataset, to avoid noisy displacement values due to glacier retreat. The Randolph Glacier Inventory (RGI v.6) was used as the source of glacier outlines (RGI Consortium, 2017).

c) Additionally, median surface displacement value was subtracted from the total displacement fields on both east-west (EW) and north-south (NS) displacement maps for all dates. Median value was computed over the entire EW and NS products computing each one for their specific dates.

d) For the L7/8 dataset, striping effects from sensor inter-band misalignments (Ayoub et al., 2008; Leprince et al., 2008) were mitigated by subtracting the median value of the stacked profile in the along-stripe direction, considering only stable areas (cf. Section 4.3).

e) A least-squares inversion was applied to the redundant displacement pairs for each pixel, separately for EW and NS components (Bontemps et al., 2018). This process reduced uncertainties by approximately 30%, as shown in prior applications on SPOT 1-4 images. A weight strategy can be added to the different pairs during the inversion, to take into account the surface-cover changes over time. Due to the arid and natural cover of our area of study, this weight is not used here.

4.2 Automatic extraction of PMAs

The time series of cumulative surface displacements from L7/8 images are then used to automatically extract PMAs. The PMA are a group of connected pixels having a coherent movement in time and following the downslope direction, as this is expected for motions driven by gravity (rock glaciers, landslides) or other erosive processes (i.e. shifting rivers, river banks erosion). Briefly, this methodology, developed by Stumpf et al., (2017), proposes to use the direction coherence of the displacement (called the vector coherence) with time to detect active pixels. A TanDEM-X World DEM with 12 m

resolution, smoothed with 7x7 windows size (approximately 90 m) was used to compute the slope orientation to detect pixels consistent with gravitational movements. Namely we remove pixels whose mean velocity vectors are oriented less than 45° from the downslope direction calculated over a kernel size of 200 m to take into account the relatively large-scale undulations of the topography. These relatively high parameters have been chosen after a series of trials, and take into account the lower resolution of the images used compared to Stumpf et al., (2017), and the presence of snow in high mountains that can alter the quality of the displacement fields. Following this pixel-based approach, isolated pixels are removed.

4.3 PMA characterisation using InSAR and high resolution imagery

As mentioned in Section 3.3, InSAR wrapped interferograms were used mainly for validation and characterization of automatic PMA detection. Rather than create a new inventory of moving areas, we manually checked all polygons resulting from PMA methodology (cf. Section 4.2) against the interferograms. As suggested in Barboux et al., (2014) and RGIK, (2023), we used a combination of all available interferograms (Table S2) with high resolution Google Earth imagery to classify slope movements. During this analysis, we consider the PMA confirmed when the polygons overlap a clear InSAR fringe pattern at any interval (e.g. 12, 60 and 360 days) on the interferograms (Fig. 3). The analysis resulted in a binary class, 'confirmed' and 'not confirmed'. Secondly, a simple geomorphological class based on high resolution Google Earth imagery was assigned to each polygon. The geomorphological class reflects the landform overlapping the PMA polygon. For instance, a landslide class was assigned when cracks and scarps were present at the surface. Rock glacier class was assigned when typical morphology i.e. front and lateral margins with ridge-and-furrow surface topography was observed. When no clear interpretation about the movement and the geomorphology interpretation could be assessed on either InSAR or Google-Earth basemaps, the PMA was classified within the 'other' geomorphological class. These features are often located not so far from the ridges and at the valley bottom (i.e. river banks erosion, road construction, …). Finally, we also assigned a velocity class for each PMA, based on RGIK, (2023) recommendations (cf. Section 6.2).

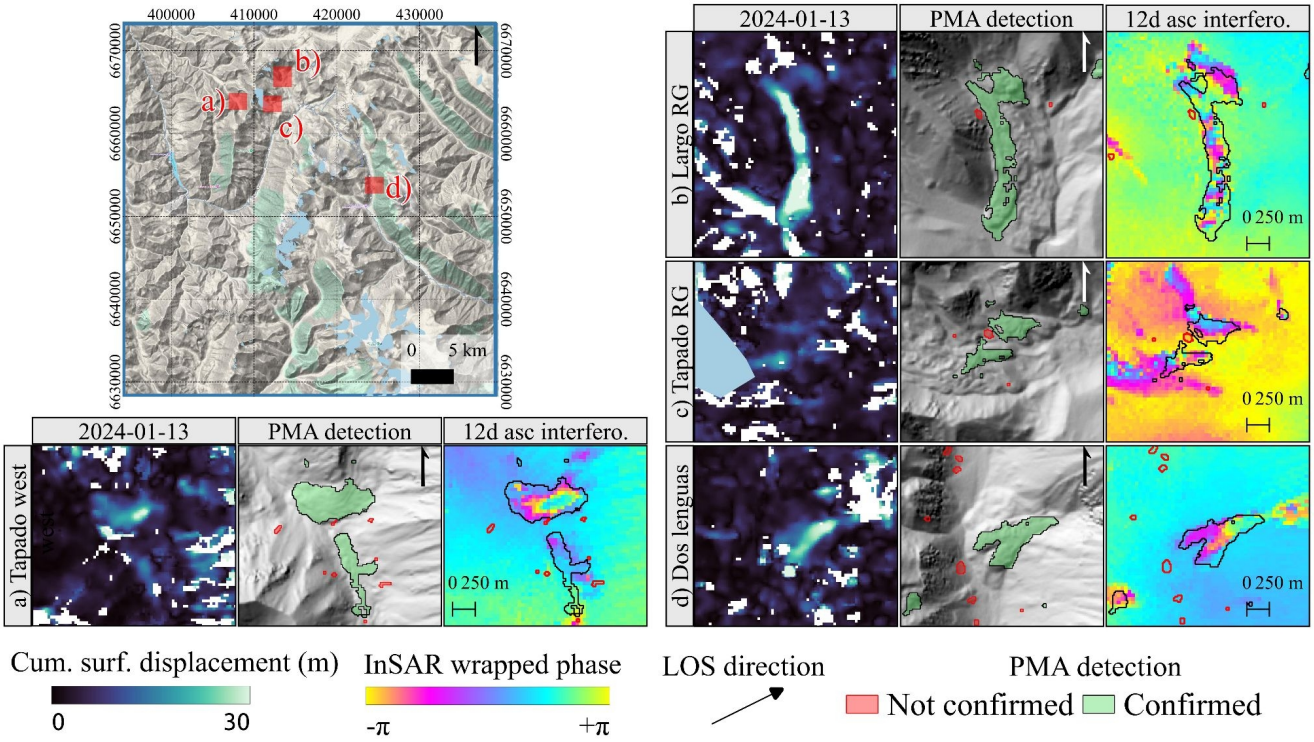

Figure 3: Example of raw outputs from inversion time-series, PMAs detection and PMAs validation using InSAR wrapped interferograms. Upper left map shows the location of small inner maps a) Tapado west, b) Largo RG, c) Tapago complex and d) Dos Lenguas. Image background corresponds to © GoogleTerrain. For all inner maps from left to right, show cumulative surface displacement map after inversion time-series last date available. In the middle, PMA's detection after directional and magnitude filtering and at right, 12 days ascending S-1 wrapped interferograms. Red and green polygons represent raw 'non confirmed' and 'confirmed' PMAs.

4.4 Average spatial velocity and relative velocity changes

Average velocity field was estimated using a linear fit of the cumulative surface displacements per pixel though time. Then, the representative surface velocity was extracted for each confirmed PMA. The most common approach to obtain average representative surface velocity values is to use the most active portion, often situated in proximity to the central profile (RGIK, 2023). This avoids the potential for lateral variability within the landform (Fig. 3). For instance, Kääb et al., (2021) employed a small area on the most active sectors to express the representative velocity for the entire rock glacier. Nevertheless, the selection of this 'active' area remains somewhat subjective and may vary between users. In other respects, Blöthe et al., (2020) proposed the selection of pixels at the 95th percentile above the limit of detection (LoD) to remove the lateral effects. As shown in Fig. 3a to d, the pixels located in the borders often have values close to 0 m a^{-1}, due mainly to natural geomorphological causes (i.e. increased friction and low/no ice content in lateral margins) as well as to window sizes

of feature-tracking algorithms. So, the boundary effect for each PMA can bias the average velocity. To mitigate this bias, we propose a similar metric than Blöthe et al., (2020) to keep only the Top 50% pixels within each PMA (hereafter referred to as Top 50% average velocity) to represent the average spatial velocity for each PMA. Refer to Section 6.3 for a more detailed discussion.

Uncertainties of surface displacement and velocity fields were computed using the Normalised Mean Absolute Deviation (NMAD; Höhle and Höhle, 2009) over stable areas. Stable areas were defined using TanDEM-X DEM and slopes lower than 35°, without taking into account neither glacier outlines with a buffer of 500 m for each glacier (RGI Consortium, 2017) nor all PMAs, also not confirmed ones produced in this study (Fig. S4). In this sense, stable areas correspond to 53% of the entire study area i.e. 45x45 km² (Fig. S4).

In this study, relative velocity changes between two periods are considered and can be calculated using Equation 1, by using the first period as the reference. The related uncertainties of the relative velocity change can be calculated using Equation 2, assuming that the NMAD for both periods are not so different (σV). Finally, from Eq. 1 and Eq. 2 we estimate a pixel-based relative velocity change and their related uncertainty, for each PMA.

$$V_{change} = \frac{V_2 - V_1}{V_1} \quad (1)$$

$$\sigma V_{change} = \left(\frac{V_2 + V_1}{V_1^2} \right) * \sigma V \,, \quad (2)$$

5 Results

5.1 Characterization of PMA extraction

Within the area of interest covered by the L7/8 dataset the automatic PMA detection produced 1710 polygons of moving objects. The raw PMAs area ranges from 225 to ~755,000 m² (Fig. 4). All PMA were verified based on InSAR and optical cross-check validation (cf. Section 4.3). From this analysis, 29% of PMA were classified as 'confirmed' (nb = 501). Within the 'confirmed' PMAs, we classified 42% of the PMA as rock glaciers, 32% as landslides and 26% polygons classified as 'other'. Among the 42% of rock glaciers, we identified six rock glaciers directly connected to a debris-covered glacier. We decided to keep those within the 'rock glacier' class rather than create a separate class because the PMA essentially covers only the rock glacier component. Table 1 summarises all features and classes identified through the interpretation analysis. On the other hand, 71% of PMAs (n = 1209) were classified as 'not confirmed' because no clear interpretation could be obtained from Google Earth optical imagery and interferograms. Within the 'not confirmed' PMAs, 10% (n = 116) of PMA corresponds to the glacier class and thus, directly removed.

Table 1: Summary of raw PMA geomorphological characterisation through cross-check verification using S1 InSAR and Google Earth optical imagery (cf. Section 4.3). Information about their statistical distribution is presented in Figure S1.

TOTAL POLYGONS		Manual characterization		Above automatic surface threshold (2250 m² - 10 pixels)	
		n	%	**n**	%
Confirmation class	Geomoph class	1710	100	975	100
NOT CONFIRMED by InSAR	Sub total	1209	71	593	61
	Other	747	62	382	64
	valley bottom	159	13	77	13
	ridges	155	13	79	13
	landslide	17	1	14	2
	rock glacier	15	1	5	1
	glaciers	116	10	77	13
CONFIRMED by InSAR	Sub total	501	29	382	39
	rock glacier	211	42	153	40
	Landslide	160	32	105	27
	Other	130	26	124	32

During the manual characterization process, we noticed the presence of an important number of small and isolated polygons within the 'not confirmed' class (Fig. 4), often located close to the mountain ridges and at the valley bottom (Fig. S3). As these tiny polygons cannot be correctly interpreted, we set up a surface threshold of 2250 m² (i.e. 10 pixels), to remove them automatically. The threshold of 10 pixels has been selected on the basis of PMA size and their corresponding InSAR fringe pattern (cf. Section 3.3; Fig. 3), becoming difficult to interpret below this threshold. By using this surface threshold, 43% (n = 735) of the all PMAs were removed from the analysis..

The selected surface threshold seems to be a good compromise to remove noisy (smaller) PMA and keep coherent (larger) PMAs, by only compromising 15% of confirmed PMA (Fig. 4). After the surface threshold is applied and PMA corresponding to glacier class were removed, the remaining filtered dataset containing 901 PMA (47% of the initial dataset), only 39% (n = 382) of PMA are confirmed. Those PMA correspond mostly to large gravitational mass movements among rock glaciers, landslides and other mass movements (Tab. 1). The confirmed PMAs have a mean surface of ~30,000 m² (Fig. S3). The remaining 61% (n = 519) of not confirmed PMA also represent a consistent group of pixels which potentially represents a gravitational movement, but these could not be validated within the cross-check methodology (cf. Section 4.3). Those have a mean area size of 8,000 m² equivalent to 35 pixels. These polygons are often isolated and located close to the mountain ridges, or at the valley floor. From Figure 4 we can also state that the ratio between confirmed and not-confirmed

PMAs increases when PMA are bigger, suggesting that larger the object size, the higher the likelihood of PMA detection using the L7/8 dataset. Further discussion regarding the possible causes of these polygons can be found in Section 6.2. For the rest of the manuscript, we will only take into account the 382 valid polygons (i.e. after applying the surface threshold).

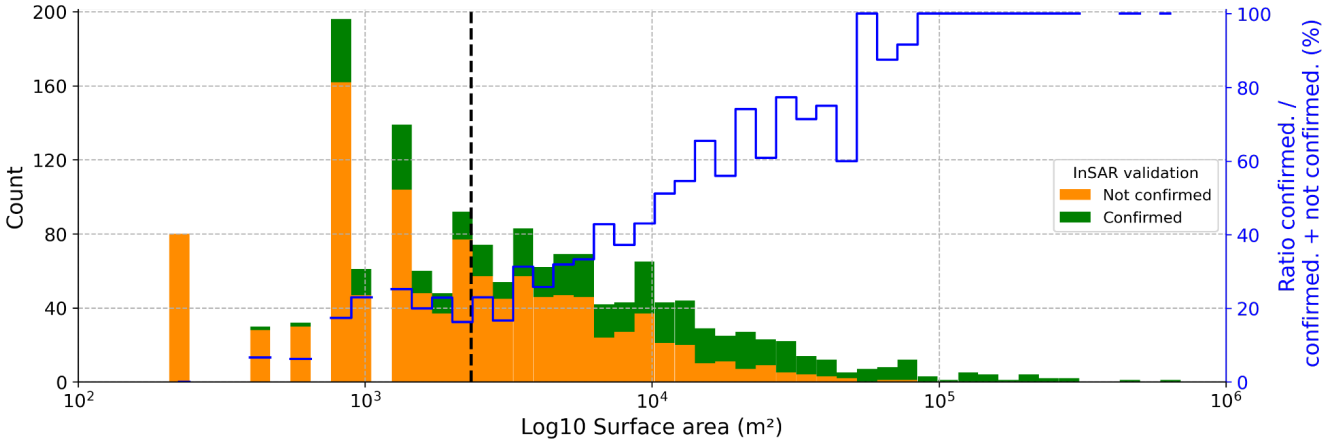

Figure 4: Distribution of raw 'confirmed' and 'not confirmed' PMA by surface area (bins = 50). Black vertical line represents the surface threshold i.e. 2250 m² (10 pixels) used as a filter to remove smaller PMAs. All polygons below the surface threshold were removed. Blue line, represents the ratio between valid features over total features by bins. For access to our PMA polygons for our own assessment, refer to the Data availability section.

5.2 Regional distribution of surface velocity

Figure 5a provides an overview of the 24-year average velocity within the central Andes region. For each PMA, we obtain a coherent downward surface velocity field overlapping a sector of a rock glacier (cf. Section 6.3 for discussion). The Top 50% average velocity corresponds to 0.30 m a^{-1} over 24 years of displacements for all 382 PMAs. The NMAD computed over stable areas corresponds to ±0.07 m a^{-1} over 24 years. Refer to Section 5.4 for a discussion about the uncertainties.

The Top 50% average velocities independent for each geomorphological class —rock glaciers, landslides, and others— correspond to 0.37 m a^{-1}, 0.20 m a^{-1} and 0.18 m a^{-1}, respectively. Among the classes, rock glaciers clearly show a median average velocity higher (+23%) than the average velocity for the entire PMA dataset (Fig. S9. Only three PMA have Top 50% average velocities greater than 2 m a^{-1}, corresponding to the Largo rock glacier (Fig. 2c; Fig. 5c), Olivares and Olivares west complex rock glaciers (Fig. 4f and g) and one landslide; and only eight PMAs have Top 50% average velocities between 1 – 2 m a^{-1}, corresponding to five relatively large rock glaciers and three landslides. The rest of the PMA dataset (n = 371) has average velocities below 1 m a^{-1} over 24 years.

In addition to the average velocity field, we were also able to obtain cumulative displacement time series (Fig. 5) of all PMAs (Fig. S9) over 24 years. The displacements time series are useful to depict temporal changes such as changes in velocity, e.g. accelerations or decelerations (Fig. 5e and f). Most of the rock glaciers (those with mean velocities < 1 m a^{-1}), show a linear trend of surface displacements (Fig. 5b and d). Depicting annual velocity changes is rather challenging because the average NMAD for all individual velocity pairs on stable areas corresponds to 1.18 m a^{-1} (Table 2). In some cases, particularly for the fastest and biggest PMAs, some accelerations (Fig. 5e) and deceleration (Fig. 5f) could be qualitatively assessed. Given the large uncertainties at annual scale, the observed accelerations are not statistically significant for most of the PMAs (cf. Section 5.4).

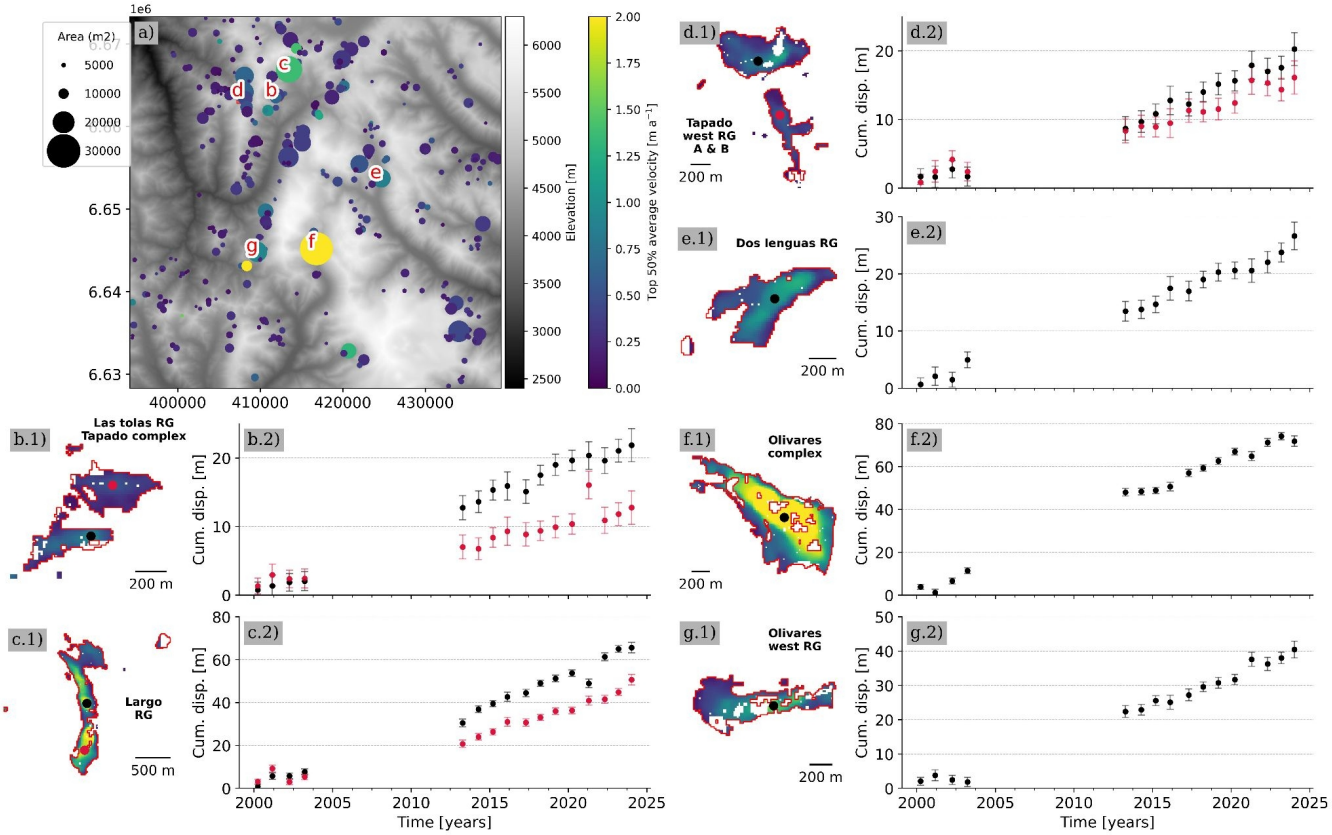

385 **Figure 5:** Surface kinematic characterisation for all PMAs in the central Andes region. a) Illustrates the spatial distribution of all valid PMAs (rock glaciers = 146; landslides = 115; others = 103) coloured by the 'Top 50% average velocity' surface velocity (viridis colorbar) within the PMA surface. The size of the circle is proportional to the rescaled PMA surface in m²/1,000 for better visualisation. The red letters correspond to the study cases presented in the following subplots. The remaining subplots b) to g) (with a suffix of *.1) illustrate mean annual velocity field over the 24 years (2000-2024) for a 390 specific landform (name is displayed in bold) where the magnitude of velocity is coloured using viridis colorbar from panel a). Subplots with a suffix of *.2 represents the cumulative surface displacement time series in metres (subplots with a suffix of *.2), extracted on the black (and red) point within the landform. Cumulative error bars were computed NMAD on stable areas for each date respectively (Section 5.4). Subplots b) to g) correspond to the following landforms b) Tapado Complex and Las Tolas Rock Glacier; c) Largo Rock Glacier; d) Tapado west Rock Glacier; e) Dos Lenguas Rock Glacier; f) Olivares 395 Complex, g) Olivares west Rock Glacier.

5.3 Velocity validation using GNSS and VHR datasets

We compare surface velocity fields in more detail for the two selected sub-regions around the Tapado and Largo rock glaciers (Fig. 2a). A first comparison was made between GNSS points distributed along the main tongue of Tapado complex

and Largo rock glacier and L7/8 and VHR surface average velocity fields. Both GNSS points and pseudo-GCPs are located in the central flow line as well as the border of the landform (Figure 6). This point to pixel comparison is shown in Figure 7 from where a good agreement between VHR and GNSS and pseudo-GCPs exist. Some slight differences (i.e. underestimation of average velocity) could be observed notably on those points located on the borders of the Tapado complex and Largo rock glacier. In addition, some of the fastest points on the Largo rock glacier also present important differences. Regarding specifically the comparison between L7/8 and GNSS datasets, in the Tapado complex, both average velocities agree relatively well (Fig. 7). For the Largo rock glacier, the difference in average velocity is important because the average velocity field is more heterogeneous. The points located in the borders do not fit with the pseudo-GCPs (cf. Section 5.4 for a quantitative assessment).

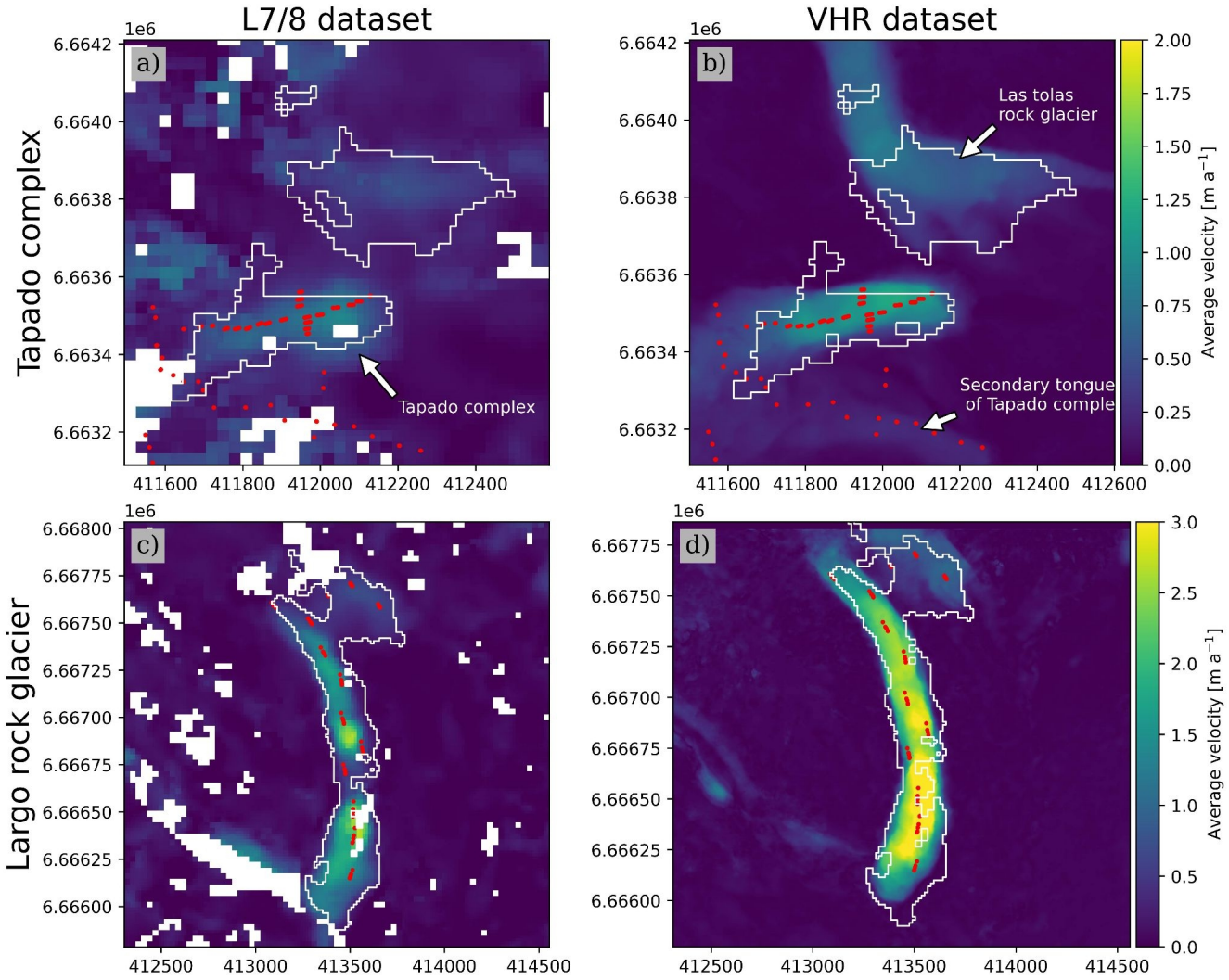

Figure 6: Comparison of mean annual velocity over the 2000-2020 period for Tapado complex a) and b); and Largo rock glacier c) and d) for both L7/8 and VHR dataset, respectively. Red points show the location of GNSS for Tapado complex (CEAZA, 2023) and pseudo-GCP for Largo rock glacier. White polygons correspond to their respective PMA identified from the L7/8 dataset (cf. Section 3.5).

Quantitatively, the average differences in velocity between VHR and GNSS points is about 0.01 ± 0.05 m a^{-1} (Tapado complex) and 0.38 ± 0.3 m a^{-1} (Largo rock glacier) while, the average difference between L7/8 and GNSS points is 0.18 ± 0.24 m a^{-1} (Tapado complex) and 1.35 ± 0.84 m a^{-1} (Largo rock glacier; Figure 7). The good agreement on slow surface velocities on the Tapado complex could be explained by the homogeneous surface velocity field in both datasets (Fig. 6a). However, this is not the case on the Largo rock glacier where large differences could be likely explained by the

heterogeneous surface velocity field from L7/8. Figure 6c shows a single PMA that could be either divided in two, splitting Largo rock glacier in two different units, with likely independent dynamics. This is not the case for the VHR velocity field, showing rather a more homogeneous spatial distribution of velocities (Fig. 6d).

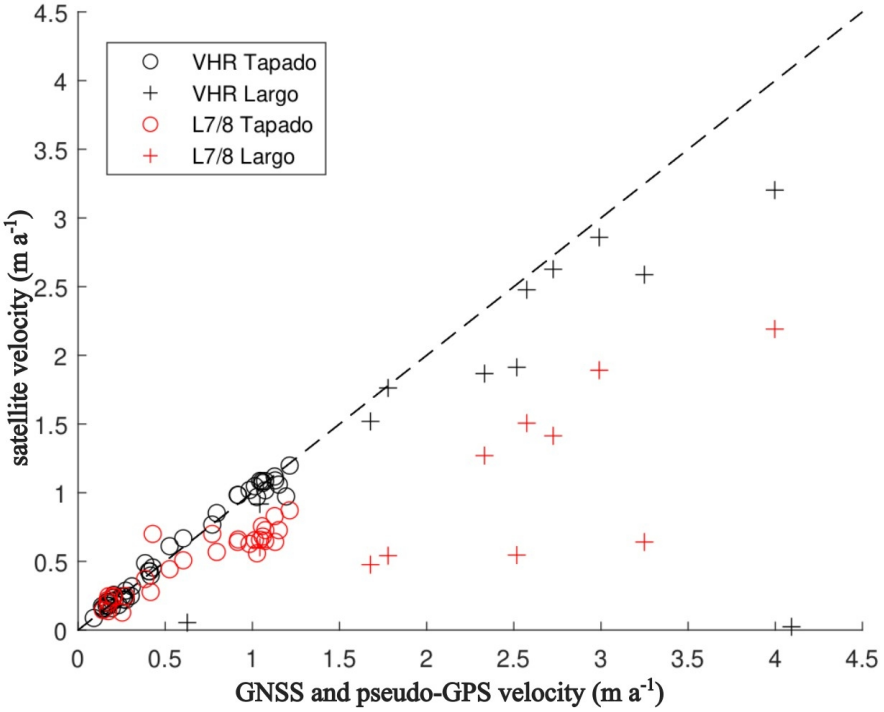

Figure 7: Comparison between GNSS, pseudo-GCPs points average velocity and average surface velocity fields from inversion time series for both L7/8 and VHR datasets in the subregions of Tapado complex and Largo rock glacier. The average surface velocities from GNSS measurements, L7/8 and VHR datasets, were calculated according to the common time period, spanning from 2009 to 2020.

A detailed comparison with VHR optical imagery revealed a good agreement with GNSS data. The correlation coefficient of 0.99 and 0.45 was obtained for the Tapado and Largo rock glaciers respectively and the coefficient of the linear fit between VHR and GNSS of 0.99 and 0.44 over the Tapado and Largo). The lower values of the Largo rock glacier are due to those points situated in the rock glacier borders (Fig. 6 and Fig. 7). The correlation between L7/8 and GNSS data is also very good, especially for the Tapado (0.92 and 0.7 for the Tapado and Largo respectively) but, L7/8 tends to always underestimate the velocities (coefficient of the linear fit of 0.69 and 0.45 for the Tapado and Largo rock glaciers). In terms of velocity magnitude, the Tapado and Las Tolas rock glaciers do not present large differences. The L7/8 dataset tends to

slightly underestimate surface velocities up to 20% over those landforms. Please refer to Section 6.1 for further discussion about the possible causes of the underestimations.

5.4 Reported uncertainties

The horizontal accuracy assessment at annual and selected periods in this study is summarized in Table 2. For the L7/8 dataset, the average NMAD of consecutive surface displacement over stable areas obtained is 1.8 m in EW and NS components. Uncertainties are slightly greater in recent years due to the cumulative error of time series (Table 2). The average median value over stable areas corresponds roughly to 1/10 of L7/8 pixel size. For consecutive annual surface velocities, the average NMAD is 1.18 m a^{-1}. As expected, annual uncertainties are too high to reliably detect statistically significant changes in velocity at annual scale. At decadal time spans, uncertainties decrease significantly (Table 2). The NMAD is 0.11 and 0.13 m a^{-1}, for 2000-2014 and 2013-2024 periods, respectively. Again, applying the average NMAD value for both periods as a filter of PMAs, 150 PMAs are above this threshold, being good candidates to depict velocity changes. Finally, as the 'Top 50 average velocity' of all PMA is 0.3 m a^{-1}, at decadal scale and uncertainties encompasses 43% of the overall average velocity.

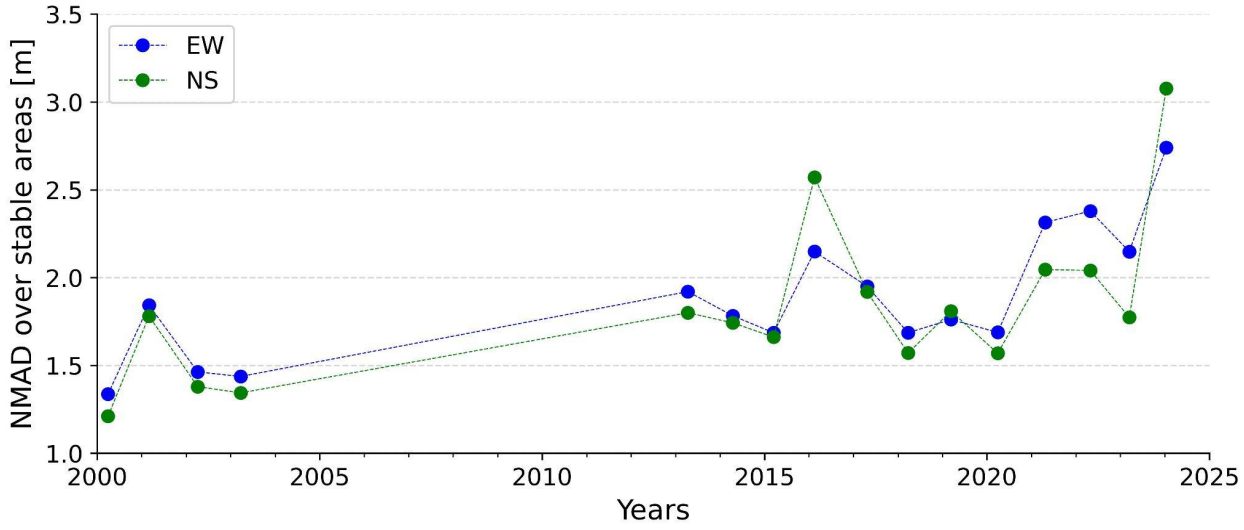

Figure 8. Annual NMAD values for the east-west (EW) and north-south (NS) components over stable areas for the L7/8 dataset. Figure S4 presents the stable area map of the study area used for NMAD computing.

Table 2. Accuracy assessment of surface displacement and surface velocity maps at annual and decadal time span. Spatial statistics were computed over a stable area of 53% for L7/8 (n pix = 4 810045), 55 % (n pix = 10 593 874) and 47% (n pix =

3 522 115) for Tapado complex and Largo rock glacier VHR dataset. [(a)] Values between brackets represent the range (min and max) values over a stable area for each component. [(b)] Difference velocity between GNSS and pseudo-GCPs vs surface velocity fields, computed using the same time period. [(c)] VHR dataset was split in two sub periods trying to fit the same time span as for the L7/8 dataset.

		STABLE AREAS								MOVING AREAS	
		Annual surface displacement [m] [(a)]		Decadal velocity [m a^{-1}]				24-year velocity [m a^{-1}]		Difference in velocity [m a^{-1}] [(b)]	
				2000-2014		2013-2024		2000-2024		2010-2022	
L7/8 dataset		E-W	N-S	E-W	N-S	E-W	N-S	E-W	N-S	Tapado	Largo
	Mean	[-0.16, 0.45]	[-0.70, 0.20]	-0.009	-0.009	0.032	-0.021	0.004	-0.008	0.183	1.359
	Median	[-0.36, 0.32]	[-0.82, 0.34]	-0.006	-0.014	0.017	-0.023	0.004	-0.015	0.157	1.224
	Std	[2.25, 5.93]	[2.37, 6.03]	0.275	0.298	0.255	0.283	0.136	0.141	0.236	0.837
	Nmad	[1.33, 2.74]	[1.21, 3.07]	0.150	0.148	0.148	0.120	0.093	0.084	0.240	1.001
		Multi annual surface displacement [m] [(a)]		Decadal velocity [m a^{-1}] [(c)]				20-year velocity [m a^{-1}]		20-year velocity [m a^{-1}]	
				2000-2014		2012-2020		2000-2020		2010-2022	
VHR dataset		E-W	N-S	E-W	N-S	E-W	N-S	E-W	N-S	Tapado	Largo
	Mean	[-0.05, 0.11]	[0.19, 0.06]	0.010	-0.012	-0.002	-0.006	0.005	0.002	0.011	0.377
	Median	[-0.23, 0.0]	[-0.23, 0.06]	-0.011	-0.020	-0.002	0.000	-0.012	-0.012	0.006	0.206
	Std	[0.35, 1.34]	[0.31, 1.16]	0.120	0.097	0.049	0.054	0.078	0.065	0.047	0.307
	Nmad	[0.11, 0.36]	[0.28, 1.00]	0.030	0.078	0.030	0.010	0.020	0.048	0.036	0.133

5.5 Velocity changes

Using the 24-year surface displacement dataset, decadal velocity changes were analyzed by calculating surface velocities over two periods: 2000–2014 (V_1) and 2013–2024 (V_2), for all PMAs. The uncertainty in velocity change depends on the magnitude of velocity in both periods (Eq. 2). Smaller velocity magnitudes result in greater relative uncertainties (Eq. 2). To illustrate, a velocity increase from 0.5 to 1.0 m a^{-1} (100% change) has an uncertainty of 0.78 m a^{-1}, representing 78% of the relative change. In contrast, an increase from 1.0 to 2.0 m a^{-1} has an uncertainty of 0.39 m a^{-1}, or 39% of the relative velocity change. Consequently, only PMAs with velocities exceeding 1 m a^{-1} can be considered reliable for statistically significant velocity change. By considering PMAs with velocities exceeding 1 m a^{-1}, nine ‘rock glaciers’ and 2 ‘landslides’. Within those selected features, three rock glaciers showed an increase in velocity 11% (Fig. 5c), whereas six rock glaciers showed a decrease in velocity of 18% over two decades. On the other hand, two Landslides exhibited a larger increase in velocity of 50%. For further discussion, please refer to Section 6.5.

6 Discussion

Rock glacier velocities are commonly estimated using high resolution optical data (e.g. Pellet et al., 2022) and SAR remote sensing imagery (Strozzi et al., 2020, Villarroel et al., 2018), but these datasets are relatively recent, covering only the past 20 years (Toth & Jóźków, 2016). In contrast, Landsat imagery (e.g. L4-5-7 or L8) extends back to the mid-1980s (Kooistra et al., 2024; Ustin and Middleton, 2021). However, VHR and freely available SAR datasets are often limited in accessibility and can be prohibitively expensive for larger areas. In this context, freely accessible L7/8 imagery emerges as a valuable source of information for studying rock glacier dynamics over extensive spatial and temporal scales (Lacroix et al., 2020b). To the best of our knowledge, this is the first time that Landsat imagery is being employed to monitor rock glacier displacement time series and derive velocities. This analysis is enabled by combining robust methods, including redundancy of information, inversion of time series and the persistent moving area detection, which make L7/8 data viable for rock glacier monitoring. Nonetheless, several aspects must be discussed in order to account for the limitations, but also perspectives of the use of Landsat imagery for rock glacier kinematics analysis.

6.1 Intrinsic limitations on the remote sensing datasets

The primary technical point for consideration is the spatial resolution of the L7/8 dataset (i.e. 15 m in the panchromatic band). Given that the pixel size is relatively coarse relative to the region's average surface velocity (i.e. ~1 m $a^{-1;}$ Vivero et al., 2021; Halla et al., 2021), this method is best suited for large, fast-moving rock glaciers. Thus, in areas with sizable rock glaciers, such as the Andes or High Mountain of Asia (Sun et al., 2024), medium-resolution L7/8 imagery can offer new insights into the temporal dynamics of rock glaciers. This suitability largely depends on rock glacier size, and pixel coverage within the landform (Section 5.1). Here, a minimum surface threshold of 2250 m² (10 pixels) proves effective for the Andes, but perhaps less so for other regions with smaller rock glaciers as the European Alps, which may fall below the detection threshold. The 15 m spatial resolution limits the ability to capture fine details, making it challenging to discern small-scale spatial variations in velocity. Figure 6 illustrates how pixel size affects boundary delineation: in the Tapado complex, the secondary tongue (Fig. 6a, b) —moving at 0.25–0.5 m a^{-1} (Vivero et al., 2021)— appears indistinct and shows gaps and noise in displacement fields (Fig. 6a), as does the adjacent Las Tolas rock glacier. Despite this, the automatic PMA extraction (Section 3.4) successfully identifies a coherent PMA across much of Las Tolas' tongue (Fig. 6a), demonstrating this filter's potential for detecting active rock glaciers even at high altitudes, where snow and shadows introduce noise in image correlation (Cusicanqui et al., 2023).

Another key consideration is the surface roughness and texture of the rock glacier, which appear less detailed in L7/8 than the VHR dataset. Surface features like ridges and furrows (Fig. 2c) can both enhance or complicate image matching due to self-similarity, impacting feature tracking performance (Kääb & Heid, 2012). For example, on the main tongue of the Tapado complex (Fig. 6a), L7/8-derived surface velocity is consistent with GNSS data (0.01 ± 0.05 m a^{-1}). The 24-year

average surface velocities align with Vivero et al., (2021) but show a discrepancy of 0.1–0.2 m a^{-1}, likely due to L7/8 image resolution. Similar differences occur on the Dos Lenguas rock glacier, which has an average velocity of 1.5–2 m a^{-1} (Halla et al., 2020; Strozzi et al., 2020), while L7/8 imagery shows average velocities of 1.1–1.5 m a^{-1} (Fig. 5e). In contrast, Largo rock glacier presents more complexity. Despite its ridge and furrow morphology, its homogeneous texture (Fig. 2d) limits contrast, potentially explaining observed discrepancies between the L7/8 and VHS results for average surface velocities (3–4 m $a^{-1;}$ Figure 6b). The resolution of L7/8 images, which capture less surface detail, affects velocity estimations within landforms with high internal variability. Therefore, the choice of correlation parameters are key when performing image correlation (Kääb & Heid, 2012; Leprince et al., 2008; Rosu et al., 2015). As L7/8's smallest matching window (3x3 pixels, covering 2025 m²) differs substantially from the VHR window (7x7 pixels, covering 49 m²) leading to an averaging effect. This difference contributes to the observed variability within the same features like Largo rock glacier. Finally, changes in solar illumination can introduce shadow-induced noise in image correlation (Dehecq et al., 2015), which we minimised by selecting L7/8 images mainly from March (with a few from January).

6.2 Validation of PMA using InSAR and local rock glacier inventories

The average velocity fields from L7/8 optical satellite data align reasonably well with Sentinel-1 interferograms and their interpretation. Figure 9 visually compares InSAR wrapped interferograms and PMA characterisation. While S1 interferograms show only LOS motion, limiting discrimination of lateral and vertical movements (Barboux et al., 2014), optical imagery provides both horizontal components of surface kinematics. Regarding the binary classification (i.e. 'confirmed' and 'not confirmed'), PMAs are based on quantitative measurement; however, there is uncertainty/ambiguity in the InSAR activity classes and PMA velocity range classifications. First, some PMAs cover complex landforms with diffuse boundaries, and thus were assigned a general geomorphological class without specific discrimination, including debris-covered glacier and glacier-rock glacier transitions (Monnier & Kinnard, 2015, 2016). Secondly, PMAs categorized as 'other' geomorphological classes lack clear geomorphological features for full interpretation. Not confirmed PMAs, often located in low-relief areas, near riverbeds, or close to ridges (Fig. S2), likely due to the smoothed DEM used as slope direction reference, or shadows in L7/8 images. Some other PMAs were found near human settlements, including mining sites, where InSAR did not indicate displacement.

The combined use of radar and optical data at the time of classification influences the assigned velocity class. InSAR velocity class for each PMA were assigned following RGIK (2023), though FLATSIM interferograms have a coarser pixel size (i.e. 30 m) than those in Strotzi et al., (2020) or Bertone et al., (2021), sometimes making fringe patterns barely discernible, specially for small landforms. In addition, interferograms reflect LOS movements over short time intervals (e.g. 12 days, 60 days, etc) with a limited time-period (2022-2023), potentially missing gravitational movements that were inactive at that time.

Rock glaciers are slightly better detected than other features like landslides, likely due to the lower motion variability over time. Indeed, rock glaciers are viscous flows (Haeberli et al., 2006) that face changes of activity over long periods of time (Kellerer-Pirklbauer et al., 2022; Lehmann et al., 2021). On the contrary, landslides can be influenced by seasonal and transient patterns (Lacroix et al., 2020b).

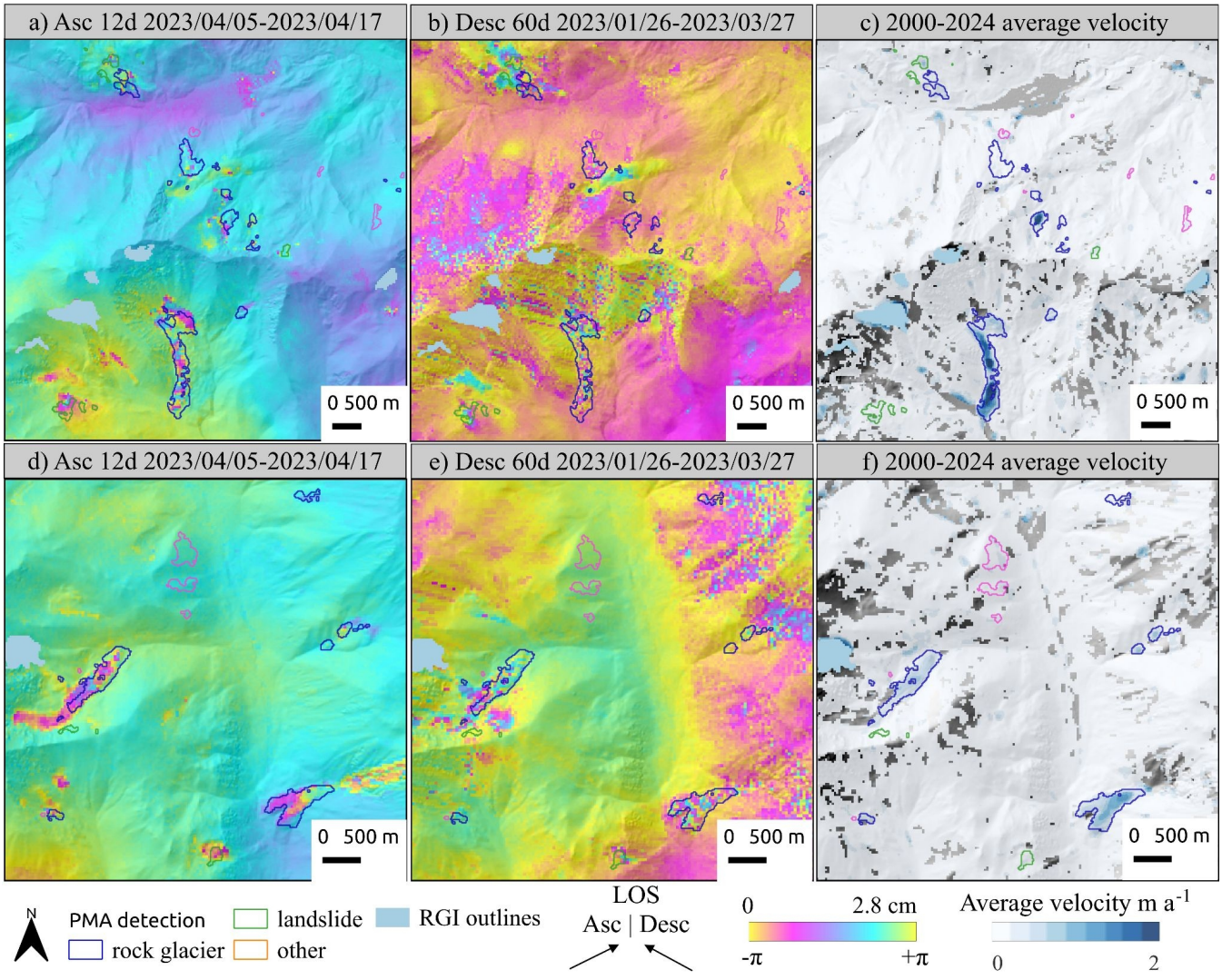

Figure 9: Comparison between Sentinel-1 wrapped interferograms at 12 and 60 days of interval and average surface velocity fields, in two small regions in the Central Andes.

A comparison was conducted between the two existing rock glacier inventories for the Chilean (DGA, 2022) and Argentinian (IANIGLA, 2018) Andes, focusing on PMAs classified as rock glaciers only (nb = 153). Using Ch-Arg rock

glacier inventory as a reference, 68% of the PMAs (nb = 104) intersects the existing inventory at an average of 30% of their surface area (Fig. S12). However, only 20% of the overlapping PMA (nb = 20) overlaps the inventory by more than 50% of their surface. The remaining 32% of the PMA (nb = 49) comprises unmapped rock glaciers, identified through L7/8 optical imagery and validated with InSAR (RGIK, 2023). This comparison relies on the accuracy of the Ch-Arg rock glacier inventories, which contains certain ambiguities. For instance, the Chilean inventory, released in 2013 and updated in 2022 (DGA, 2022), shows an overrepresentation of the rock glaciers, by including some headwall sections (Fig. S12), while the Argentinian inventory, defines rock glacier limits more conservatively. Neither of the two inventories has been updated yet in accordance with the RGIK guidelines (RGIK, 2023). Finally, regarding the PMA activity class classified as rock glaciers, InSAR velocity data indicate that 69% (nb = 105) were detected using 12-day interferograms (Fig. 9f), suggesting a velocity class between 30 – 100 cm a^{-1} (RGIK, 2023), which agrees with the findings of this study.

6.3 Average PMA surface velocity

Since our dataset comprises a spatial representation of surface displacement field for 382 PMAs (comprising 153 rock glaciers, 124 landslides and 105 non-classified landforms), we can pose the following question: what is the most appropriate threshold for computing average surface velocity fields?

In our study, computing statistics per landform using the same threshold could be complex, due to the large pixel size of L7/8 imagery and the size of PMA. If we compute spatial average velocities using the Top 50% pixels, the bias resulting from lateral variability is automatically removed and an area in the middle of the PMA is conserved (see Fig. S15 for a comparison), corresponding to the fastest area (Fig. 6). This fastest area obtained from this methodology (Blöthe et al., 2021) is independent for each PMA area and is solely based on 24-year average velocity within the PMA. However, when computing spatial average velocities using different thresholds, the mean average velocity may be overestimated. Figure 10 also presents a quantitative estimation of the influence of selecting 'Top 50%, 30% and 10% average velocity. The mean difference between the average velocity over the entire PMA surface and the 'Top 50%, 30% and 10% average velocity' corresponds to 20%, 31% and 44%, respectively. These differences underscore the significance of selecting the most appropriate thresholds. Here, we consider that the 'Top 50% average velocity' computed over a 24-year period represents an optimal compromise between the average velocity field without lateral effects and the remaining amount of pixels within the PMA, with the potential to reduce the ambiguity introduced by the operator. Nevertheless, further studies should be conducted to evaluate this metric using different temporal intervals and with different remote sensing datasets.

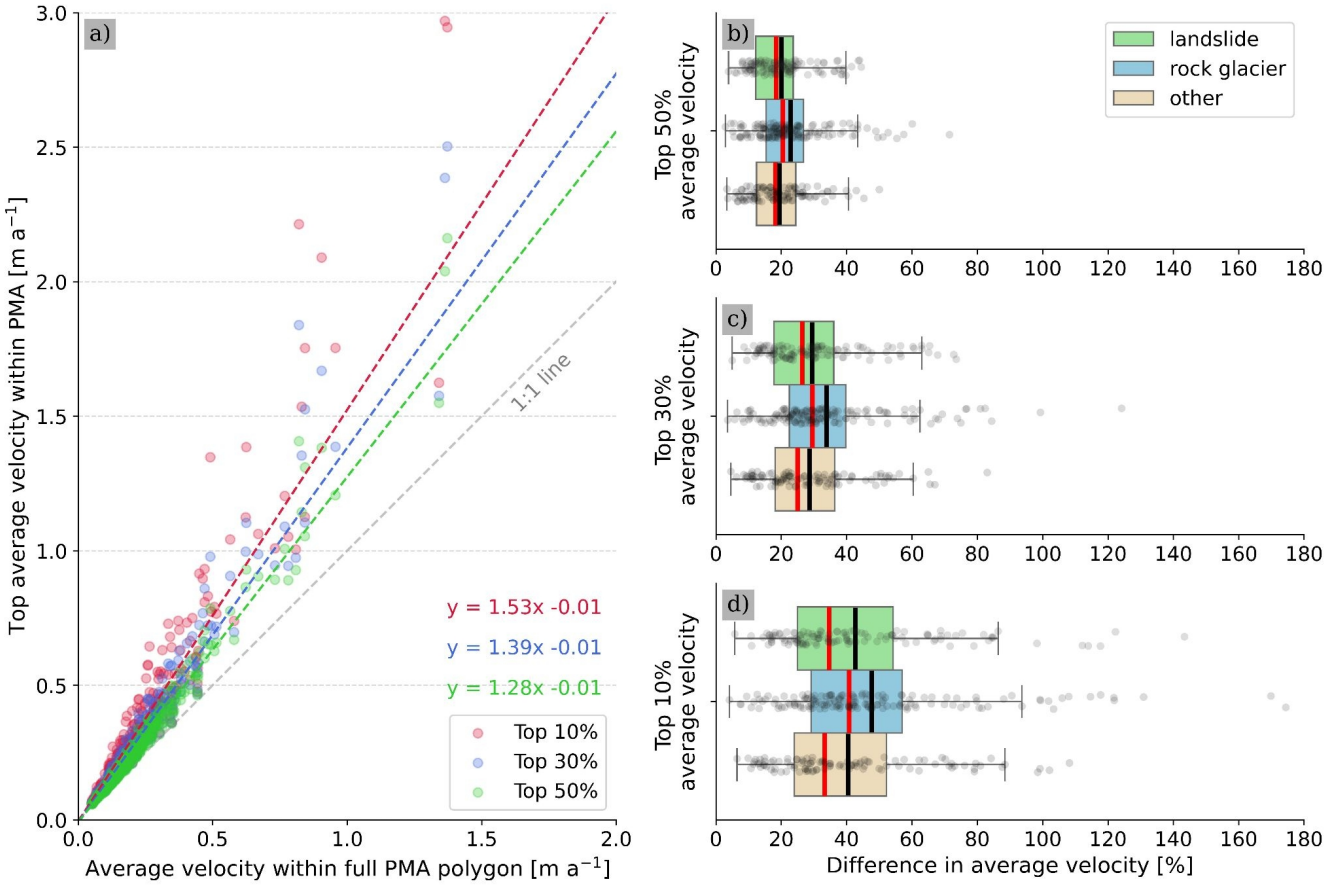

Figure 10: a) Comparison between average velocity computed using the entire PMA surface and 'Top 50%, 30% and 10% average velocity' within PMA. Subplots b), c), and d) show the difference of average velocity 'Top 50%, 30% and 10% average velocity' in respect to the average velocity computed over the entire PMA surface.

6.4 Surface velocity variations and uncertainties

Regarding uncertainties in those PMA with GNSS data —Tapado and Largo rock glaciers— our approach generally underestimates surface velocities by 10–20% on average (Fig. 7). Tapado surface velocities (1–2 m a^{-1}) align well with GNSS data, but Largo surface velocities (2–4 m a^{-1}) are underestimated by 30–40%, likely due to textural differences and lack of contrast on L7/8 dataset (Section 6.1). The general underestimation of surface velocities in L7/8 imagery could be attributed to the large pixel size (15 m), which reduces pixel counts per matching window. Gaps between 2003 and 2013 may also introduce biases on displacement time series. Velocities were validated only on two of the 382 PMAs using in situ measurements or VHR imagery, raising questions about the validity of the remaining rock glaciers measurements. Calculations show an NMAD over stable areas of 0.07 m a^{-1} ± 0.16 as standard deviation (over 24-year period), similar to the uncertainties found by Kääb et al., (2021) in the Tien Shan region using high-resolution historical images with poor scan

quality. In contrast, Blöthe et al., (2021), using a Limits of Detection (LoD) method with high-resolution optical images, reported uncertainties from 0.28 to 0.5 m a^{-1}. The low uncertainties reported in the L7/8 imagery, computed over a 24-year period, brings confidence in the interpretation.

However, annual velocity uncertainties are notably higher than those estimated over the entire period. The mean ± standard deviation NMAD over stable areas (Fig. S3) for consecutive displacements is 1.8 m ± 0.33 and 1.18 m a^{-1} ± 0.44, consistent with values reported in previous studies (Lacroix et al., 2019; Scherler et al., 2008), using L7/8 images. Applying the mean NMAD as LoD filter (Blöthe et al., 2021) only 2% of PMAs (n = 8) above the threshold were retained, corresponding to large and fast rock glaciers (Fig. 5c, f, and g). This analysis demonstrates that L7/8 imagery allows kinematic characterization over large periods of time (10-20 years) but not annual velocity variations. Further studies are required to enhance our understanding of the annual velocity changes observed using L7/8 images.

Decadal velocity changes between 2000-2014 and 2013-2024 (Eq. 1) raise questions about the representativeness given velocity uncertainties (Eq. 2). Three main factors contribute:

- Observation discrepancies: The 2000 to 2014 period includes only six years of observations due to a gap between 2003 and 2013, whereas 2013 to 2024 has 11 years of continuous observations. This may bias the average velocity for each period, conditioning related uncertainties (Fig. 5). The use of ASTER images or other medium-resolution data could help to fill this gap despite the low radiometric resolution (Lacroix et al., 2020).
- PMA size: L7/8 imagery performs better on larger landforms with more moving pixels. As high uncertainties of velocity change are present on borders of PMAs due to the small velocity magnitude, the border effect is less pronounced on bigger PMAs than the smaller ones. However, larger PMAs obtained in this study are landforms related to complex processes (glacier-permafrost interactions) which may have been influenced by internal landform variability. Largo rock glacier experienced a change in velocity of +54% and +29% in L7/8 and VHR datasets, respectively. Conversely, Olivares ice-debris complex (debris-covered glacier connected), showed a -9% velocity change in one decade the L7/8 data. Similar patterns observed were observed 100 km south if Elqui valley (Monnier et al., 2014; Monnier and Kinnard, 2013, 2015), as well as in the Tien Shan region (Kääb et al., 2021), the European Alps (Cusicanqui et al., 2023; Gärtner-Roer et al., 2021; Kunz and Kneisel, 2020). All these observations suggest that complex interaction between glacier retreat and permafrost-related landforms influence surface velocities in contiguous landforms, highlighting areas for further research.
- Andean velocity observations: Limited Andean studies report few changes in recent decades. Vivero et al., (2021) found a 7% of acceleration in the 2000-2020 decade. Our VHR data show limited changes, with -3 ± 10 % slow-down in the Tapado rock glacier and +14 ± 10 % speed-up in Largo rock glacier between 2000-2010 and 2010-2020 Over 40 years, Vivero et al. (2021) observed a 0.2 m a^{-1} acceleration in Tapado rock glacier, representing 25% of velocity increase in average. Such a level of acceleration might not be detected by L7/8 imagery. Further studies

could benefit from incorporating older datasets, like SPOT 1-4 up to the mid 1980's or Corona images from the 1960s (Dehecq et al., 2020).

6.5 Wider geomorphic implications of PMAs

Understanding the broader geomorphic implications of PMAs is critical for interpreting their role within high mountain environments and their response to climatic and geomorphological processes. While much of the manuscript focuses on kinematic and spatial characteristics of PMAs, this section aims to contextualize the observed patterns within a regional framework, bridging findings with topographic and geomorphological contexts, shedding light on the factors influencing their spatial distribution and surface dynamics. The PMAs in the study area show heterogeneous spatial distribution across topographic conditions (Fig. 5a). Analysis of the Top 50% average velocity and its relationship to slope, aspect, elevation and surface area, derived from the TanDEM-X 12.5 m DEM, reveals several key patterns (Fig. 11, Fig. S7)

- Rock glaciers are generally found on slopes 10–35°, while 'landslides' and 'other' features are concentrated on slopes steeper than 25°, peaking at 30° and 35°, respectively. This pattern aligns with the regional slope distribution, suggesting a control of slope for landslides and other landforms (Fig. 11a).
- Slope aspect distributions vary distinctly between feature types. Rock glaciers primarily face West to South and East, consistent with regional permafrost models (Gruber, 2012, Obu, 2021; Azocar et al., 2017). In contrast, landslides and other features are predominant on north-west to east slopes (Fig. 11d). Similar findings from Blothë et al., (2021) in the Cordon del Plata also emphasize slope orientation as a controlling factor.
- Most of the rock glaciers with velocities between 1–2 m a^{-1} are located at altitudes of 4,500–5,000 m a.s.l., although no strong correlation with altitude was found. In contrast, 'landslide' and 'others' PMAs occur at lower elevations (around 3500 m a.s.l.), often where the presence of permafrost is heterogeneous or discontinuous (Gruber 2012; Azócar et al., 2017) (Fig. 11b).
- In the Top 50% average velocity category, larger rock glaciers exhibit higher surface velocities, unlike 'landslide' and 'others' categories (Fig. 11c). This may reflect specific and local geomorphological context, such as the accumulation zone at Largo rock glacier, which likely drives material influx (Janke and Frauenfelder, 2008) and surface acceleration (+54% in the L7/8 dataset). By contrast, Olivares ice-debris complex shows deceleration, potentially linked to ice-mass loss in adjacent debris-covered glaciers. Similar patterns have been observed in the Tien Shan region (Kääb et al., 2021) and more recently in the European Alps (Manchado et al., 2024). More detailed studies are necessary to understand the mechanics of these complex landforms.

Although the objective of our study is the monitoring of rock glaciers on a regional scale, other PMAs corresponding to mass movements such as landslides could also be identified. Our results suggest possible correlations between gravitational movements in high mountain areas (e.g. Haeberli et al., 2017; Patton et al., 2019) and permafrost degradation (i.e. freeze, thaw of permafrost) in recent deglaciated areas (Pánek et al., 2022). This study allows us to complete those existing mass

movement inventories in the region (e.g. Iribarren Anacona et al., 2015), highlighting areas for further research. While these findings suggest useful regional relationships between surface kinematics and topographic parameters at the regional scale, they must be interpreted cautiously. The morphological statistics here are derived only within PMA boundaries and may not fully represent the whole landform (Fig. S12). Additionally, PMAs exclude feeder basins, responsible for material supply and water to the rock glacier (Blöthe et al., 2021; Cusicanqui et al., 2021). Further studies should be conducted to look at the influences of feeder basins on surface kinematics of rock glaciers.

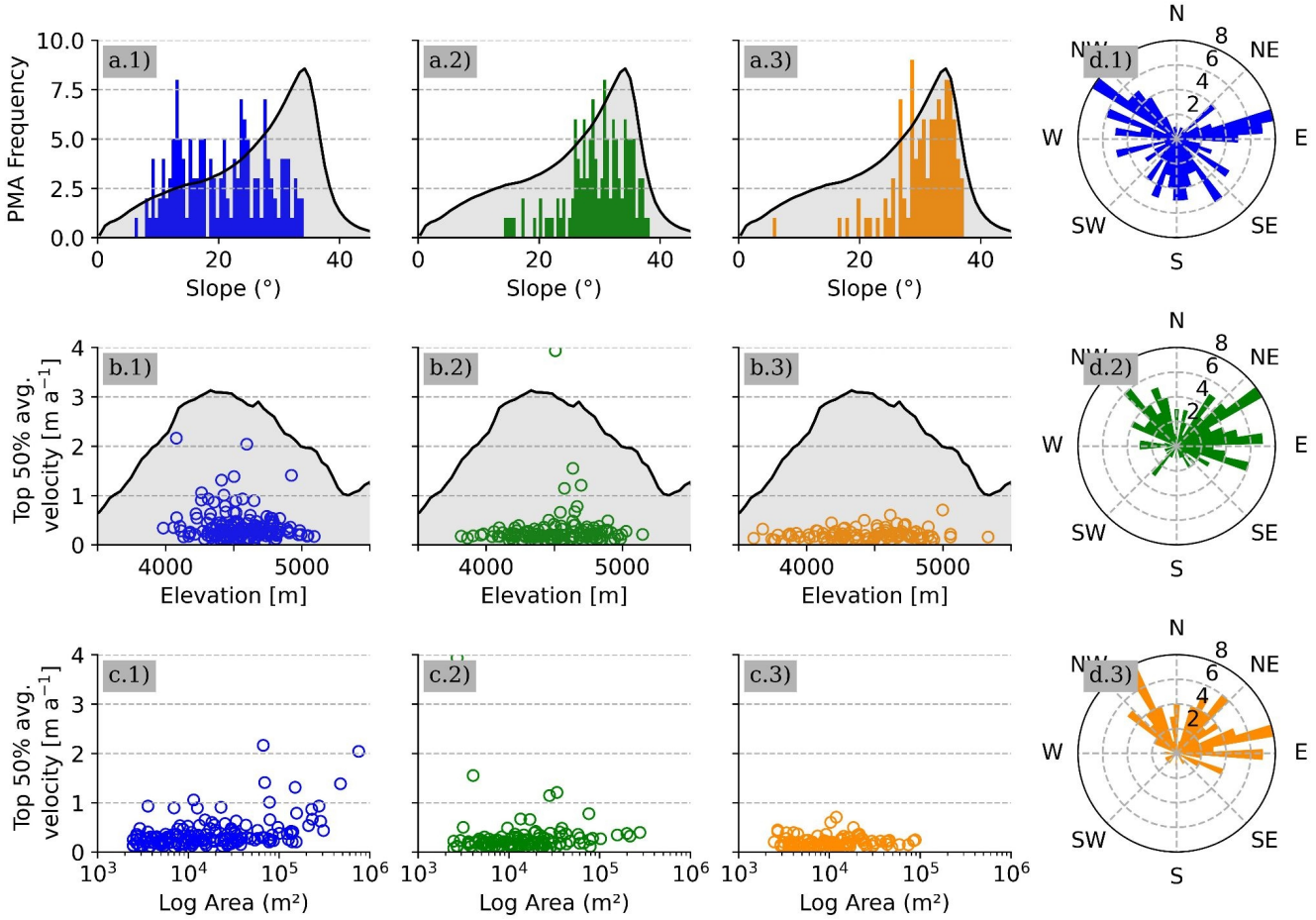

Figure 11: Comparison of the PMA distribution for 'rock glacier' (blue values), 'landslide' (green values) and 'other' (orange values) geomorphological class vs regional topographical context (computed using average pixel frequency from TanDEM-X 12 m DEM). a) PMA mean slope; b) distribution between Top 50% average velocity PMA and PMA mean elevation; c) distribution between Top 50% average velocity and PMA surface; d) PMA slope orientation. For a) and b), the grey background represents the general slope and elevation context of the study area, respectively.

6 Conclusion

This study developed a robust method to detect, quantify, and analyse the surface kinematics of rock glaciers and other gravitational slope movements using time series of Landsat 7/8 imagery. By integrating feature tracking from 24 years of imagery with time series inversion and automatic detection of persistent moving areas (PMA), the study successfully monitored 382 mass movements over a 45x45 km² area in the semiarid Andes. Validation using satellite radar interferometry confirmed the classification and velocity attributes of the PMAs, with 42% also detected by Sentinel-1 interferograms at 12 days temporal baselines. Faster-moving landforms (2–4 m a^{-1}), primary complex ice-debris landforms, were detected. The 24-year average velocity was 0.3 ± 0.07 m a^{-1}, with rock glaciers moving 23% faster than the median of all types of geomorphological objects. Although underestimations occurred due to pixel size, temporal data gaps and velocity field heterogeneity, decadal velocity changes were observable under certain conditions, particularly for features exceeding 1 m a^{-1}. Below this threshold, velocity changes detected with L7/8 data were not statistically significant. The results aligned well with existing research and highlighted the potential of combining radar and optical remote sensing to improve the detection and monitoring of both slow and fast gravitational movements. The findings enhance rock glacier mapping and kinematic understanding, particularly in the context of permafrost warming and its effects on periglacial landforms. This study demonstrates the capability of medium-resolution L7/8 images for quantifying the kinematics of rock glaciers and ice-debris complex dynamics at a regional scale. It provides a methodological benchmark for assessing the state of periglacial landforms using globally accessible, open-source optical imagery, addressing a key need within the scientific community.

Code availability. Feature tracking image correlation softwares used for this study are open-source softwares. Ames Stereo Pipeline (ASP) is available from https://stereopipeline.readthedocs.io/en/latest/introduction.html (Bayer et al., 2018) and MicMac is available from https://micmac.ensg.eu/index.php/Accueil (Rupnick et al., 2017). Time-series inversion from optical imagery (TIO) is available from https://sourcesup.renater.fr/www/tio/. Sentinel-1 interferograms were computed using ForM@Ter LArge-scale multi-Temporal Sentinel-1 InterferoMetry processing chain (FLATSIM) based on the NSBAS pipeline. Both are available through GDM-SAR service at https://www.poleterresolide.fr/le-service-gdm-sar-in/.

Data availability. Landsat 7/8 archive freely available at http://earthexplorer.usgs.gov/. Sentinel-1 data used in our study are freely available from the ESA/EC Copernicus Sentinels Scientific Data Hub at https://scihub.copernicus.eu (Copernicus Open Access Hub, 2021). FLATSIM Sentinel-1 interferograms can be accessible upon request via Form@Ter pole (https://www.poleterresolide.fr/). TanDEM-X data are available from DLR through proposal application procedures. Data from Digital-Globe satellites (GeoEye, Ikonos, WorldView, Quickbird) and Pléiades are commercial, but programmes to facilitate academic access exist. Pleiades dataset can be accessed upon request to Ben Robson (Benjamin.Robson@uib.no). The data described in this manuscript are available at (https://zenodo.org/uploads/13119042; Cusicanqui et al., 2024) or upon request from the corresponding author (diego.cusicanqui@univ-grenoble-alpes.fr).

Supplement. The supplement related to this article is available online at: https://zenodo.org/uploads/13119042.

Author contributions. DC, PL and XB designed the study. DC performed image correlation of VHR data provided by BR and XB. PL performed image correlation of L7/8 data and implemented persistent moving area (PMA) detection. DC and PL filter GNSS dataset provided by SM and compute GNSS surface velocity time-series. DC wrote the paper with the supervision and contributions of PL. PL, XB, BR, AK and SM contributed to the discussion and edited the paper.

Competing interests. The authors declare that they have no conflict of interest.

Acknowledgment. Thanks are due to reviewers for their careful review and comments. We are grateful to the providers of free data for this study: European Space Agency (ESA)/European Commission (EC) Copernicus for Sentinel-1 data, the FLATSIM Form@TER team for their efforts processing Sentinel interferograms. Also, the German Aerospace Center (DLR) for providing the TanDEM-X DEM. We are grateful to CNES/Airbus DS for the provision of the SPOT and Pléiades satellite to the restrained dataset project 41743. We would like to thank the U.S. Geological Survey for making the Landsat 7/8 archive freely available. Thanks to GLIMS database http://glims.org/RGI/ for glacier outlines (v.6). All (or most of) the computations presented in this paper were performed using the GRICAD infrastructure (https://gricad.univ-grenoble-alpes.fr), which is supported by Grenoble research communities. Thanks to the glaciology group at CEAZA for collecting and providing the GNSS datasets, and the CHESS-funded (https://chess.w.uib.no/) "Summer school on cryospheric monitoring and water resources" for the 2022 acquisition set.

Financial support. This work has been supported by the postdoctoral program from the National Centre for Space Studies (CNES) and partially by the National Center for Scientific Research (CNRS), the program Plan d'Action pour la Prévention des Risques d'Origine Glaciaire et périglaciaire (PAPROG). This work has also been partially supported by a grant from Labex OSUG (Investissements d'avenir – ANR10 LABX56) PermANDES project. Data provided by CEAZA was supported by ANID-CENTROS REGIONALES R20F0008. Diego Cusicanqui (CNES | ISTerre), Pascal Lacroix (IRD | ISTerre), Xavier Bodin (EDYTEM | CNRS) are part of Labex OSUG (ANR10 LABX56).

References

Arenson, L., Colgan, W., and Marshall, H. P.: Chapter 2 - Physical, Thermal, and Mechanical Properties of Snow, Ice, and Permafrost, in: Snow and Ice-Related Hazards, Risks and Disasters, edited by: Shroder, J. F., Haeberli, W., and Whiteman, C., Academic Press, Boston, 35–75, https://doi.org/10.1016/B978-0-12-394849-6.00002-0, 2015.

Arenson, L. U., Harrington, J. S., Koenig, C. E. M., and Wainstein, P. A.: Mountain Permafrost Hydrology—A Practical Review Following Studies from the Andes, Geosciences, 12, 48, https://doi.org/10.3390/geosciences12020048, 2022.

Ayoub, F., Leprince, S., Binet, R., Lewis, K. W., Aharonson, O., and Avouac, J. P.: Influence of camera distortions on satellite image registration and change detection applications: 2008 IEEE International Geoscience and Remote Sensing Symposium - Proceedings, 2008 IEEE International Geoscience and Remote Sensing Symposium - Proceedings, II1072–II1075, https://doi.org/10.1109/IGARSS.2008.4779184, 2008.

Azócar, G. F. and Brenning, A.: Hydrological and geomorphological significance of rock glaciers in the dry Andes, Chile (27°-33°S): Rock Glaciers in the Dry Andes, Permafrost Periglac. Process., 21, 42–53, https://doi.org/10.1002/ppp.669, 2010.

Azócar, G. F., Brenning, A., and Bodin, X.: Permafrost distribution modelling in the semi-arid Chilean Andes, The Cryosphere, 11, 877–890, https://doi.org/10.5194/tc-11-877-2017, 2017.

Barboux, C.: Detection, mapping and monitoring of slope movements in the Alpine environment using DInSAR., PhD, University of Fribourg, 212 pp., 2014.

Berthling, I.: Beyond confusion: Rock glaciers as cryo-conditioned landforms, Geomorphology, 131, 98–106, https://doi.org/10.1016/j.geomorph.2011.05.002, 2011.

Bertone, A., Barboux, C., Bodin, X., Bolch, T., Brardinoni, F., Caduff, R., Christiansen, H. H., Darrow, M. M., Delaloye, R., Etzelmüller, B., Humlum, O., Lambiel, C., Lilleøren, K. S., Mair, V., Pellegrinon, G., Rouyet, L., Ruiz, L., and Strozzi, T.: Incorporating InSAR kinematics into rock glacier inventories: insights from 11 regions worldwide, The Cryosphere, 16, 2769–2792, https://doi.org/10.5194/tc-16-2769-2022, 2022.

Beyer, R. A., Alexandrov, O., and McMichael, S.: The ames stereo pipeline: NASA's open source software for deriving and processing terrain data, Earth and Space Science, 5, 537–548, https://doi-org.insu.bib.cnrs.fr/10.1029/2018EA000409, 2018.

Blöthe, J. H., Halla, C., Schwalbe, E., Bottegal, E., Trombotto Liaudat, D., and Schrott, L.: Surface velocity fields of active rock glaciers and ice-debris complexes in the Central Andes of Argentina, Earth Surface Processes and Landforms, 46, 504–522, https://doi.org/10.1002/esp.5042, 2021.

Bodin, X., Thibert, E., Fabre, D., Ribolini, A., Schoeneich, P., Francou, B., Reynaud, L., and Fort, M.: Two decades of responses (1986–2006) to climate by the Laurichard rock glacier, French Alps, Permafrost Periglac. Process., 20, 331–344, https://doi.org/10.1002/ppp.665, 2009.

Bolch, T., Shea, J. M., Liu, S., Azam, F. M., Gao, Y., Gruber, S., Immerzeel, W., Kulkarni, A., Li, H., Tahir, A., Zhang, G., Zhang, Y., Bannerjee, A., Berthier, E., Brun, F., Kääb, A., Kraaijenbrink, P., Moholdt, G., Nicholson, L., Pepin, N., and Racoviteanu, A.: Status and change of the cryosphere in the Extended Hindu Kush Himalaya Region, in: The Hindu Kush

Himalaya Assessment, edited by: Wester, P., Mishra, A., Mukherji, A., and Shrestha, A. B., Springer, 209–255, https://doi.org/10.1007/978-3-319-92288-1_7, 2019.

Bontemps, N., Lacroix, P., and Doin, M.-P.: Inversion of deformation fields time-series from optical images, and application to the long term kinematics of slow-moving landslides in Peru, Remote Sensing of Environment, 210, 144–158, https://doi.org/10.1016/j.rse.2018.02.023, 2018.

Brenning, A.: Spatial prediction models for landslide hazards: review, comparison and evaluation, Nat. Hazards Earth Syst. Sci., 5, 853–862, https://doi.org/10.5194/nhess-5-853-2005, 2005.

Burger, K. C., Degenhardt, J. J., and Giardino, J. R.: Engineering geomorphology of rock glaciers, Geomorphology, 31, 93–132, https://doi.org/10.1016/S0169-555X(99)00074-4, 1999.

CEAZA: Reporte anual 2012. Avalaible at www.ceazamet.cl. Accessed on Febraury 15, 2024, 2012.

CEAZA: Reporte anual 2016. Avalaible at www.ceazamet.cl. Accessed on Febraury 15, 2024, 2016.

CEAZA: Datos meteorologicos proveidos por el CEAZA. obtenidos desde. www.ceazamet.cl. Avalaible at www.ceazamet.cl. Accessed on Febraury 15, 2024, 2023.

Cicoira, A., Beutel, J., Faillettaz, J., and Vieli, A.: Water controls the seasonal rhythm of rock glacier flow, Earth and Planetary Science Letters, 528, 115844, https://doi.org/10.1016/j.epsl.2019.115844, 2019.

Cusicanqui, D., Rabatel, A., Vincent, C., Bodin, X., Thibert, E., and Francou, B.: Interpretation of Volume and Flux Changes of the Laurichard Rock Glacier Between 1952 and 2019, French Alps, Journal of Geophysical Research: Earth Surface, 126, e2021JF006161, https://doi.org/10.1029/2021JF006161, 2021.

Cusicanqui, D., Bodin, X., Duvillard, P.-A., Schoeneich, P., Revil, A., Assier, A., Berthet, J., Peyron, M., Roudnitska, S., and Rabatel, A.: Glacier, permafrost and thermokarst interactions in Alpine terrain. Insights from seven decades of reconstructed dynamics of the Chauvet glacial and periglacial system (Southern French Alps), Earth Surface Processes and Landforms, 48, 2595–2612, https://doi.org/10.1002/esp.5650, 2023.

Dehecq, A., Gourmelen, N., and Trouve, E.: Deriving large-scale glacier velocities from a complete satellite archive: Application to the Pamir–Karakoram–Himalaya, Remote Sensing of Environment, 162, 55–66, https://doi.org/10.1016/j.rse.2015.01.031, 2015.

Dehecq, A., Gardner, A. S., Alexandrov, O., McMichael, S., Hugonnet, R., Shean, D., and Marty, M.: Automated Processing of Declassified KH-9 Hexagon Satellite Images for Global Elevation Change Analysis Since the 1970s, Front. Earth Sci., 8, https://doi.org/10.3389/feart.2020.566802, 2020.

Delaloye, R., Lambiel, C., and Gärtner-Roer, I.: Overview of rock glacier kinematics research in the Swiss Alps., Geogr. Helv., 135–145, 2010.

DGA: Dinámica de Glaciares Rocosos en el Chile Semiárido: Parte I, Plan de Monitoreo., 2010.

DGA: INVENTARIO PÚBLICO DE GLACIARES, actualización 2022. SDT N°447, 2022. Ministerio de Obras Públicas, Dirección General de Aguas Unidad de Glaciología y Nieves. Realizado por: Casassa, G., Espinoza, A., Segovia, A., Huenante, J., 2022.

Doin, M.-P., Guillaso, S., Jolivet, R., Lasserre, C., Lodge, F., Ducret, G., and Grandin, R.: Presentation of the small baseline NSBAS processing chain on a case example: The Etna deformation monitoring from 2003 to 2010 using Envisat data, in: Proceedings of the Fringe symposium, Citation Key: doin2011presentation, 3434–3437, 2011.

Etzelmüller, B., Guglielmin, M., Hauck, C., Hilbich, C., Hoelzle, M., Isaksen, K., Noetzli, J., Oliva, M., and Ramos, M.: Twenty years of European mountain permafrost dynamics—the PACE legacy, Environ. Res. Lett., 15, 104070, https://doi.org/10.1088/1748-9326/abae9d, 2020.

Facciolo, G., De Franchis, C., and Meinhardt, E.: MGM: A significantly more global matching for stereovision, in: BMVC 2015, 2015.

Garreaud, R. D., Boisier, J. P., Rondanelli, R., Montecinos, A., Sepúlveda, H. H., and Veloso-Aguila, D.: The central chile mega drought (2010–2018): A climate dynamics perspective, International Journal of Climatology, 40, 421–439, https://doi.org/10.1002/joc.6219, 2020.

Gärtner-Roer, I., Brunner, N., Delaloye, R., Haeberli, W., Kääb, A., and Thee, P.: Glacier-permafrost relations in a high-mountain environment: 5 decades of kinematic monitoring at the Gruben site, Swiss Alps, The Cryosphere Discussions, 1–30, https://doi.org/10.5194/tc-2021-208, 2021.

GCOS: Plan for the Global Climate Observing System, version 1.0., 1995.

Grandin, R.: Interferometric processing of SLC sentinel-1 TOPS data, in: FRINGE'15: Advances in the science and applications of SAR interferometry and sentinel-1 InSAR workshop, frascati, italy, 23-27 march 2015, Citation Key: grandin2015interferometric, 2015.

Gruber, S.: Derivation and analysis of a high-resolution estimate of global permafrost zonation, The Cryosphere, 6, 221–233, https://doi.org/10.5194/tc-6-221-2012, 2012.

Haberkorn, A., Kenner, R., Noetzli, J., and Phillips, M.: Changes in ground temperature and dynamics in mountain permafrost in the swiss alps, Frontiers in Earth Science, 9, https://doi.org/10.3389/feart.2021.626686, 2021.

Haeberli, W. and Gruber, S.: Global warming and mountain permafrost, in: Permafrost soils, Springer, 205–218, 2009.

Haeberli, W., Hallet, B., Arenson, L., Elconin, R., Humlum, O., Kääb, A., Kaufmann, V., Ladanyi, B., Matsuoka, N., Springman, S., and Mühll, D. V.: Permafrost creep and rock glacier dynamics, Permafrost and Periglacial Processes, 17, 189–214, https://doi.org/10.1002/ppp.561, 2006.

Haeberli, W., Schaub, Y., and Huggel, C.: Increasing risks related to landslides from degrading permafrost into new lakes in de-glaciating mountain ranges, Geomorphology, 293, 405–417, https://doi.org/10.1016/j.geomorph.2016.02.009, 2017.

Halla, C., Blöthe, J. H., Tapia Baldis, C., Trombotto Liaudat, D., Hilbich, C., Hauck, C., and Schrott, L.: Ice content and interannual water storage changes of an active rock glacier in the dry Andes of Argentina, The Cryosphere, 15, 1187–1213, https://doi.org/10.5194/tc-15-1187-2021, 2021.

Hartl, L., Fischer, A., Stocker-waldhuber, M., and Abermann, J.: Recent speed-up of an alpine rock glacier: an updated chronology of the kinematics of outer hochebenkar rock glacier based on geodetic measurements, Geografiska Annaler: Series A, Physical Geography, 98, 129–141, https://doi.org/10.1111/geoa.12127, 2016.

Hartl, L., Zieher, T., Bremer, M., Stocker-Waldhuber, M., Zahs, V., Höfle, B., Klug, C., and Cicoira, A.: Multi-sensor monitoring and data integration reveal cyclical destabilization of the Äußeres Hochebenkar rock glacier, Earth Surface Dynamics, 11, 117–147, https://doi.org/10.5194/esurf-11-117-2023, 2023.

Heid, T. and Kääb, A.: Evaluation of existing image matching methods for deriving glacier surface displacements globally from optical satellite imagery, Remote Sensing of Environment, 118, 339–355, https://doi.org/10.1016/j.rse.2011.11.024, 2012.

Hock, R., Rasul, G., Adler, C., Caceres, B., Gruber, S., Hirabayashi, Y., Jackson, M., Kääb, A., Kang, S., Kutuzov, S., Milner, Al., Molau, U., Morin, S., Orlove, B., and Steltzer, H.: High Mountain Areas. In: IPCC Special Report on the Ocean and Cryosphere in a Changing Climate [H.-O. Pörtner, D.C. Roberts, V. Masson-Delmotte, P. Zhai, M. Tignor, E. Poloczanska, K. Mintenbeck, A. Alegría, M. Nicolai, A. Okem, J. Petzold, B. Rama, N.M. Weyer (eds.)]., Cambridge University Press, Cambridge, 131–202, https://doi.org/10.1017/9781009157964.004., 2019.

Höhle, J. and Höhle, M.: Accuracy assessment of digital elevation models by means of robust statistical methods, ISPRS Journal of Photogrammetry and Remote Sensing, 64, 398–406, https://doi.org/10.1016/j.isprsjprs.2009.02.003, 2009.

Hu, Y., Harrison, S., Liu, L., and Wood, J. L.: Modelling rock glacier ice content based on InSAR-derived velocity, Khumbu and Lhotse valleys, Nepal, The Cryosphere, 17, 2305–2321, https://doi.org/10.5194/tc-17-2305-2023, 2023.

Hugonnet, R., McNabb, R., Berthier, E., Menounos, B., Nuth, C., Girod, L., Farinotti, D., Huss, M., Dussaillant, I., Brun, F., and Kääb, A.: Accelerated global glacier mass loss in the early twenty-first century, Nature, 592, 726–731, https://doi.org/10.1038/s41586-021-03436-z, 2021.

IANIGLA: Inventario Nacional de Glaciares 2018. Resumen ejecutivo de los resultados del Inventario Nacional de Glaciares. IANIGLA-CONICET, Ministerio de Ambiente y Desarrollo Sustentable de la Nacion. Pp. 27, 2018.

Janke, J. and Frauenfelder, R.: The relationship between rock glacier and contributing area parameters in the Front Range of Colorado, Journal of Quaternary Science, 23, 153–163, https://doi.org/10.1002/jqs.1133, 2008.

Janke, J., Bellisario, A., and Ferrando, F.: Classification of debris-covered glaciers and rock glaciers in the Andes of central Chile, Geomorphology, 241, https://doi.org/10.1016/j.geomorph.2015.03.034, 2015.

Jansen, F. and Hergarten, S.: Rock glacier dynamics: Stick-slip motion coupled to hydrology, Geophysical Research Letters, 33, https://doi.org/10.1029/2006GL026134, 2006.

Kääb, A., Frauenfelder, R., and Roer, I.: On the response of rockglacier creep to surface temperature increase, Global and Planetary Change, 56, 172–187, https://doi.org/10.1016/j.gloplacha.2006.07.005, 2007.

Kääb, A., Strozzi, T., Bolch, T., Caduff, R., Trefall, H., Stoffel, M., and Kokarev, A.: Inventory and changes of rock glacier creep speeds in Ile Alatau and Kungöy Ala-Too, northern Tien Shan, since the 1950s, The Cryosphere, 15, 927–949, https://doi.org/10.5194/tc-15-927-2021, 2021.

Kääb, A. and Røste, J.: Rock glaciers across the United States predominantly accelerate coincident with rise in air temperatures, Nat Commun, 15, 7581, https://doi.org/10.1038/s41467-024-52093-z, 2024.

Kalthoff, N., Bischoff-Gauß, I., Fiebig-Wittmaack, M., Fiedler, F., Thürauf, J., Novoa, E., Pizarro, C., Castillo, R., Gallardo, L., Rondanelli, R., and Kohler, M.: Mesoscale Wind Regimes in Chile at 30°S, Journal of Applied Meteorology and Climatology, 41, 953–970, https://doi.org/10.1175/1520-0450(2002)041<0953:MWRICA>2.0.CO;2, 2002.

Kaufmann, V., Kellerer-Pirklbauer, A., and Seier, G.: Conventional and UAV-Based Aerial Surveys for Long-Term Monitoring (1954–2020) of a Highly Active Rock Glacier in Austria, Frontiers in Remote Sensing, 2, 2021.

Kellerer-Pirklbauer, A. and Kaufmann, V.: About the relationship between rock glacier velocity and climate parameters in central Austria, Austrian Journal of Earth Sciences, 105, 94–112, 2012.

Kellerer-Pirklbauer, A., Lieb, G. K., and Kaufmann, V.: Rock Glaciers in the Austrian Alps: A General Overview with a Special Focus on Dösen Rock Glacier, Hohe Tauern Range, in: Landscapes and Landforms of Austria, edited by: Embleton-Hamann, C., Springer International Publishing, Cham, 393–406, https://doi.org/10.1007/978-3-030-92815-5_27, 2022.

Kellerer-Pirklbauer, A., Bodin, X., Delaloye, R., Lambiel, C., Gärtner-Roer, I., Bonnefoy-Demongeot, M., Carturan, L., Damm, B., Eulenstein, J., Fischer, A., Hartl, L., Ikeda, A., Kaufmann, V., Krainer, K., Matsuoka, N., Cella, U. M. D., Noetzli, J., Seppi, R., Scapozza, C., Schoeneich, P., Stocker-Waldhuber, M., Thibert, E., and Zumiani, M.: Acceleration and interannual variability of creep rates in mountain permafrost landforms (rock glacier velocities) in the European Alps in 1995–2022, Environmental Research Letters, 19, 034022, https://doi.org/10.1088/1748-9326/ad25a4, 2024.

Kenner, R., Phillips, M., Beutel, J., Hiller, M., Limpach, P., Pointner, E., and Volken, M.: Factors Controlling Velocity Variations at Short-Term, Seasonal and Multiyear Time Scales, Ritigraben Rock Glacier, Western Swiss Alps, Permafrost and Periglac. Process., 28, 675–684, https://doi.org/10.1002/ppp.1953, 2017.

Kenner, R., Pruessner, L., Beutel, J., Limpach, P., and Phillips, M.: Why rock glacier deformation velocities correlate with both ground temperatures and water supply at multiple temporal scales, , https://doi.org/10.5194/egusphere-egu2020-9534, 2020.

Kooistra, L., Berger, K., Brede, B., Graf, L. V., Aasen, H., Roujean, J.-L., Machwitz, M., Schlerf, M., Atzberger, C., Prikaziuk, E., Ganeva, D., Tomelleri, E., Croft, H., Reyes Muñoz, P., Garcia Millan, V., Darvishzadeh, R., Koren, G., Herrmann, I., Rozenstein, O., Belda, S., Rautiainen, M., Rune Karlsen, S., Figueira Silva, C., Cerasoli, S., Pierre, J., Tanır Kayıkçı, E., Halabuk, A., Tunc Gormus, E., Fluit, F., Cai, Z., Kycko, M., Udelhoven, T., and Verrelst, J.: Reviews and syntheses: Remotely sensed optical time series for monitoring vegetation productivity, Biogeosciences, 21, 473–511, https://doi.org/10.5194/bg-21-473-2024, 2024.

Kunz, J. and Kneisel, C.: Glacier–Permafrost Interaction at a Thrust Moraine Complex in the Glacier Forefield Muragl, Swiss Alps, Geosciences, 10, 205, https://doi.org/10.3390/geosciences10060205, 2020.

Lacroix, P., Araujo, G., Hollingsworth, J., and Taipe, E.: Self-Entrainment Motion of a Slow-Moving Landslide Inferred From Landsat-8 Time Series, Journal of Geophysical Research: Earth Surface, 124, 1201–1216, https://doi.org/10.1029/2018JF004920, 2019.

Lacroix, P., Dehecq, A., and Taipe, E.: Irrigation-triggered landslides in a Peruvian desert caused by modern intensive farming, Nat. Geosci., 13, 56–60, https://doi.org/10.1038/s41561-019-0500-x, 2020a.

Lacroix, P., Handwerger, A. L., and Bièvre, G.: Life and death of slow-moving landslides, Nat Rev Earth Environ, 1, 404–419, https://doi.org/10.1038/s43017-020-0072-8, 2020b.

Lehmann, B., Anderson, R. S., Bodin, X., Cusicanqui, D., Valla, P. G., and Carcaillet, J.: Alpine rock glacier activity over Holocene to modern timescales (western French Alps), Earth Surface Dynamics Discussions, 1–40, https://doi.org/10.5194/esurf-2022-8, 2022.

Leprince, S., Berthier, E., Ayoub, F., Delacourt, C., and Avouac, J.-P.: Monitoring Earth Surface Dynamics With Optical Imagery, Eos, Transactions American Geophysical Union, 89, 1–2, https://doi.org/10.1029/2008EO010001, 2008.

MacDonell, S., Farías, P. N., Aliste, V., Ayala, Á., Guzmán, C., Díaz, P. J., Schaffer, N., Schauwecker, S., Sproles, E. A., and Francisco, E. Y. S.: Snow and ice in the desert: reflections from a decade of connecting cryospheric science with communities in the semiarid Chilean Andes, Annals of Glaciology, 63, 158–164, https://doi.org/10.1017/aog.2023.51, 2022.

Magnin, F., Ravanel, L., Bodin, X., Deline, P., Malet, E., Krysiecki, J.-M., and Schoeneich, P.: Main results of permafrost monitoring in the French Alps through the PermaFrance network over the period 2010–2022, Permafrost and Periglacial Processes, 35, 3–23, https://doi.org/10.1002/ppp.2209, 2024.

Manchado, A. M.-T., Allen, S., Cicoira, A., Wiesmann, S., Haller, R., and Stoffel, M.: 100 years of monitoring in the Swiss National Park reveals overall decreasing rock glacier velocities, Commun Earth Environ, 5, 1–17, https://doi.org/10.1038/s43247-024-01302-0, 2024.

Marcer, M., Cicoira, A., Cusicanqui, D., Bodin, X., Echelard, T., Obregon, R., and Schoeneich, P.: Rock glaciers throughout the French Alps accelerated and destabilised since 1990 as air temperatures increased, Commun Earth Environ, 2, 1–11, https://doi.org/10.1038/s43247-021-00150-6, 2021.

Markham, B. L., Storey, J. C., Williams, D. L., and Irons, J. R.: Landsat sensor performance: history and current status, IEEE Transactions on Geoscience and Remote Sensing, 42, 2691–2694, https://doi.org/10.1109/TGRS.2004.840720, 2004.

Masiokas, M. H., Villalba, R., Luckman, B. H., Quesne, C. L., and Aravena, J. C.: Snowpack Variations in the Central Andes of Argentina and Chile, 1951–2005: Large-Scale Atmospheric Influences and Implications for Water Resources in the Region, Journal of Climate, 19, 6334–6352, https://doi.org/10.1175/JCLI3969.1, 2006.

Masiokas, M. H., Villalba, R., Luckman, B. H., and Mauget, S.: Intra- to Multidecadal Variations of Snowpack and Streamflow Records in the Andes of Chile and Argentina between 30° and 37°S, Journal of Hydrometeorology, 11, 822–831, https://doi.org/10.1175/2010JHM1191.1, 2010.

Monnier, S. and Kinnard, C.: Reconsidering the glacier to rock glacier transformation problem: New insights from the central Andes of Chile, Geomorphology, 238, 47–55, https://doi.org/10.1016/j.geomorph.2015.02.025, 2015.

Monnier, S. and Kinnard, C.: Interrogating the time and processes of development of the Las Liebres rock glacier, central Chilean Andes, using a numerical flow model, Earth Surface Processes and Landforms, 41, 1884–1893, https://doi.org/10.1002/esp.3956, 2016.

Monnier, S. and Kinnard, C.: Internal structure and composition of a rock glacier in the Andes (upper Choapa valley, Chile) using borehole information and ground-penetrating radar, Annals of Glaciology, 54, 61–72, https://doi.org/10.3189/2013AoG64A107, 2013.

Monnier, S., Kinnard, C., Surazakov, A., and Bossy, W.: Geomorphology, internal structure, and successive development of a glacier foreland in the semiarid Chilean Andes (Cerro Tapado, upper Elqui Valley, 30 08′ S., 69 55′ W.), Geomorphology, 207, 126–140, 2014.

Montecinos, A. and Aceituno, P.: Seasonality of the ENSO-Related rainfall variability in central chile and associated circulation anomalies, Journal of Climate, 16, 281–296, https://doi.org/10.1175/1520-0442(2003)016<0281:SOTERR>2.0.CO;2, 2003.

Müller, J., Vieli, A., and Gärtner-Roer, I.: Rockglaciers on the run - Understanding rockglacier landform evolution and recent changes from numerical flow modeling, The Cryosphere Discussions, 1–40, https://doi.org/10.5194/tc-2016-35, 2016.

Navarro, G., MacDonell, S., and Valois, R.: A conceptual hydrological model of semiarid Andean headwater systems in Chile, Progress in Physical Geography: Earth and Environment, 47, 668–686, https://doi.org/10.1177/03091333221147649, 2023a.

Navarro, G., Valois, R., MacDonell, S., de Pasquale, G., and Díaz, J. P.: Internal structure and water routing of an ice-debris landform assemblage using multiple geophysical methods in the semiarid Andes, Frontiers in Earth Science, 11, https://doi.org/10.3389/feart.2023.1102620, 2023b.

Noetzli, J., Biskaborn, B. K., Christiansen, H. H., Isaksen, K., Schoeneich, P., Smith, P., Vieira, G., Zhao, L., and Streletskiy, D. A.: Permafrost thermal state. In Bull. Amer. Meteor. Soc. Vol. 100., in: State of Climate 2018, vol. 9, Bull. Amer. Meteor. Soc., 21–22, 2019.

Notarnicola, C.: Hotspots of snow cover changes in global mountain regions over 2000–2018, Remote Sensing of Environment, 243, 111781, https://doi.org/10.1016/j.rse.2020.111781, 2020.

Nuth, C. and Kääb, A.: Co-registration and bias corrections of satellite elevation data sets for quantifying glacier thickness change, The Cryosphere, 5, 271–290, https://doi.org/10.5194/tc-5-271-2011, 2011.

Obu, J.: How Much of the Earth's Surface is Underlain by Permafrost?, Journal of Geophysical Research: Earth Surface, 126, e2021JF006123, https://doi.org/10.1029/2021JF006123, 2021.

de Pasquale, G., Valois, R., Schaffer, N., and MacDonell, S.: Contrasting geophysical signatures of a relict and an intact Andean rock glacier, The Cryosphere, 16, 1579–1596, https://doi.org/10.5194/tc-16-1579-2022, 2022.

Patton, A. I., Rathburn, S. L., and Capps, D. M.: Landslide response to climate change in permafrost regions, Geomorphology, 340, 116–128, https://doi.org/10.1016/j.geomorph.2019.04.029, 2019.

Pellet, C., Bodin, X., Cusicanqui, D., Delaloye, R., Kaab, A., Kaufmann, V., Noetzli, J., Thibert, E., Vivero, S., and Kellerer-Pirklbauer, A.: Rock glacier velocity, Bull. Amer. Meteor. Soc., 103, Si-S465, https://doi.org/10.1175/2022BAMSStateoftheClimate.1, 2022.

Poblete, A. G. and Minetti, J. L.: ¿Influye el calentamiento global en la disminución de las nevadas en los Andes Áridos?, Revista Universitaria de Geografía, 26, 11–29, 2017.

Réveillet, M., MacDonell, S., Gascoin, S., Kinnard, C., Lhermitte, S., and Schaffer, N.: Impact of forcing on sublimation simulations for a high mountain catchment in the semiarid Andes, The Cryosphere, 14, 147–163, https://doi.org/10.5194/tc-14-147-2020, 2020.

RGI Consortium: Randolph Glacier Inventory – A Dataset of Global Glacier Outlines: Version 6.0: Technical Report, Global Land Ice Measurements from Space., https://doi.org/10.7265/N5-RGI-60, 2017.

RGIK: Guidelines for inventorying rock glaciers, https://doi.org/10.51363/unifr.srr.2023.002, 2023.

Robson, B. A., MacDonell, S., Ayala, Á., Bolch, T., Nielsen, P. R., and Vivero, S.: Glacier and rock glacier changes since the 1950s in the La Laguna catchment, Chile, The Cryosphere, 16, 647–665, https://doi.org/10.5194/tc-16-647-2022, 2022.

Rosu, A.-M., Pierrot-Deseilligny, M., Delorme, A., Binet, R., and Klinger, Y.: Measurement of ground displacement from optical satellite image correlation using the free open-source software MicMac, ISPRS Journal of Photogrammetry and Remote Sensing, 100, 48–59, https://doi.org/10.1016/j.isprsjprs.2014.03.002, 2015.

Rupnik, E., Daakir, M., and Pierrot Deseilligny, M.: MicMac – a free, open-source solution for photogrammetry, Open Geospatial Data, Software and Standards, 2, 14, https://doi.org/10.1186/s40965-017-0027-2, 2017.

Schaffer, N. and MacDonell, S.: Brief communication: A framework to classify glaciers for water resource evaluation and management in the Southern Andes, The Cryosphere, 16, 1779–1791, https://doi.org/10.5194/tc-16-1779-2022, 2022.

Schaffer, N., MacDonell, S., Réveillet, M., Yáñez, E., and Valois, R.: Rock glaciers as a water resource in a changing climate in the semiarid Chilean Andes, Reg Environ Change, 19, 1263–1279, https://doi.org/10.1007/s10113-018-01459-3, 2019.

Schauwecker, S., Palma, G., MacDonell, S., Ayala, Á., and Viale, M.: The Snowline and 0°C Isotherm Altitudes During Precipitation Events in the Dry Subtropical Chilean Andes as Seen by Citizen Science, Surface Stations, and ERA5 Reanalysis Data, Front. Earth Sci., 10, https://doi.org/10.3389/feart.2022.875795, 2022.

Scherler, D., Leprince, S., and Strecker, M. R.: Glacier-surface velocities in alpine terrain from optical satellite imagery—Accuracy improvement and quality assessment, Remote Sensing of Environment, 112, 3806–3819, https://doi.org/10.1016/j.rse.2008.05.018, 2008.

Smith, M. J.: Chapter Eight - Digital Mapping: Visualisation, Interpretation and Quantification of Landforms, in: Developments in Earth Surface Processes, vol. 15, edited by: Smith, M. J., Paron, P., and Griffiths, J. S., Elsevier, 225–251, https://doi.org/10.1016/B978-0-444-53446-0.00008-2, 2011.

Sorg, A., Kääb, A., Roesch, A., Bigler, C., and Stoffel, M.: Contrasting responses of Central Asian rock glaciers to global warming, Scientific Reports, 5, 8228, https://doi.org/10.1038/srep08228, 2015.

Stammler, M., Cusicanqui, D., Bell, R., Robson, B., Bodin, X., Blöthe, J., and Schrott, L.: Vertical surface change signals of rock glaciers: combining UAV and Pléiades imagery (Agua Negra, Argentina), https://doi.org/10.52381/ICOP2024.138.1, 2024.

Strozzi, T., Caduff, R., Jones, N., Barboux, C., Delaloye, R., Bodin, X., Kääb, A., Mätzler, E., and Schrott, L.: Monitoring Rock Glacier Kinematics with Satellite Synthetic Aperture Radar, Remote Sensing, 12, 559, https://doi.org/10.3390/rs12030559, 2020.

Stumpf, A., Malet, J.-P., and Delacourt, C.: Correlation of satellite image time-series for the detection and monitoring of slow-moving landslides, Remote Sensing of Environment, 189, 40–55, https://doi.org/10.1016/j.rse.2016.11.007, 2017.

Sun, Z., Hu, Y., Racoviteanu, A., Liu, L., Harrison, S., Wang, X., Cai, J., Guo, X., He, Y., and Yuan, H.: TPRoGI: a comprehensive rock glacier inventory for the Tibetan Plateau using deep learning, Earth System Science Data Discussions, 1–32, https://doi.org/10.5194/essd-2024-28, 2024.

Thibert, E. and Bodin, X.: Changes in surface velocities over four decades on the Laurichard rock glacier (French Alps), Permafrost and Periglacial Processes, 33, 323–335, https://doi.org/10.1002/ppp.2159, 2022.

Thollard, F., Clesse, D., Doin, M.-P., Donadieu, J., Durand, P., Grandin, R., Lasserre, C., Laurent, C., Deschamps-Ostanciaux, E., Pathier, E., Pointal, E., Proy, C., and Specht, B.: FLATSIM: The ForM@Ter LArge-Scale Multi-Temporal Sentinel-1 InterferoMetry Service, Remote Sensing, 13, 3734, https://doi.org/10.3390/rs13183734, 2021.

Toth, C. and Jóźków, G.: Remote sensing platforms and sensors: A survey, ISPRS Journal of Photogrammetry and Remote Sensing, 115, 22–36, https://doi.org/10.1016/j.isprsjprs.2015.10.004, 2016.

Trombotto, D., Buk, E., and Hernández, J.: Rock glaciers in the southern central Andes (approx. 33–34 S), Cordillera Frontal, Mendoza, Argentina, Bamberger Geographische Schriften, 19, 145–173, 1999.

Ustin, S. L. and Middleton, E. M.: Current and near-term advances in Earth observation for ecological applications, Ecological Processes, 10, 1, https://doi.org/10.1186/s13717-020-00255-4, 2021.

Villarroel, C., Tamburini Beliveau, G., Forte, A., Monserrat, O., Morvillo, M., Villarroel, C. D., Tamburini Beliveau, G., Forte, A. P., Monserrat, O., and Morvillo, M.: DInSAR for a Regional Inventory of Active Rock Glaciers in the Dry Andes Mountains of Argentina and Chile with Sentinel-1 Data, Remote Sensing, 10, 1588, https://doi.org/10.3390/rs10101588, 2018.

Vivero, S., Bodin, X., Farías-Barahona, D., MacDonell, S., Schaffer, N., Robson, B. A., and Lambiel, C.: Combination of aerial, satellite, and UAV photogrammetry for quantifying rock glacier kinematics in the dry andes of chile (30°S) since the 1950s, Frontiers in Remote Sensing, 2, https://doi.org/10.3389/frsen.2021.784015, 2021.

Wagner, T., Kainz, S., Krainer, K., and Winkler, G.: Storage-discharge characteristics of an active rock glacier catchment in the Innere Ölgrube, Austrian Alps, Hydrological Processes, 35, e14210, https://doi.org/10.1002/hyp.14210, 2021.

Wirz, V., Geertsema, M., Gruber, S., and Purves, R. S.: Temporal variability of diverse mountain permafrost slope movements derived from multi-year daily GPS data, Mattertal, Switzerland, Landslides, 13, 67–83, https://doi.org/10.1007/s10346-014-0544-3, 2016.

Hu, Y., et al. (15 co-authors). Rock Glacier Velocity as a new product of the Essential Climate Variable Permafrost. Fernández, J., Bonsoms, J., García-Oteyza, J., & Oliva, M. (Eds.) (2023): 6th European Conference on Permafrost – Book of Abstracts, 18 June – 22 June 2023, Puigcerdà, 308. https://doi.org/10.52381/EUCOP6.abstracts.1, 2023